Universiteit Leiden
The Netherlands

The MAGPI Survey: impact of environment on the total internal mass distribution of galaxies in the last 5 Gyr

Derkenne, C.; McDermid, R.M.; Poci, A.; Mendel, J.T.; D'Eugenio, F.; Jeon, S.; ... ; Yi, S.K.

Citation

Derkenne, C., McDermid, R. M., Poci, A., Mendel, J. T., D'Eugenio, F., Jeon, S., ... Yi, S. K. (2023). The MAGPI Survey: impact of environment on the total internal mass distribution of galaxies in the last 5 Gyr. *Monthly Notices Of The Royal Astronomical Society*, *522*(3), 3602-3626. doi:10.1093/mnras/stad1079

Version: Publisher's Version

License: Creative Commons CC BY 4.0 license

Downloaded from: https://hdl.handle.net/1887/3719184

Note: To cite this publication please use the final published version (if applicable).

Monthly Notices of the ROYAL ASTRONOMICAL SOCIETY
MNRAS **522,** 3602–3626 (2023) https://doi.org/10.1093/mnras/stad1079

The MAGPI Survey: impact of environment on the total internal mass distribution of galaxies in the last 5 Gyr

Caro Derkenne,[1,2★] Richard M. McDermid,[1,2] Adriano Poci,[3] J. Trevor Mendel,[2,4] Francesco D'Eugenio,[5,6] Seyoung Jeon,[7] Rhea-Silvia Remus,[8] Sabine Bellstedt,[9] Andrew J. Battisti,[2,4] Joss Bland-Hawthorn,[2,10] Anna Ferré-Mateu,[11,12] Caroline Foster,[2,13] K. E. Harborne,[2,9] Claudia D.P. Lagos,[9,14] Yingjie Peng,[15,16] Piyush Sharda,[2,4,17] Gauri Sharma,[18,19,20] Sarah Sweet,[2,21] Kim-Vy H. Tran,[2,13] Lucas M. Valenzuela,[8] Sam Vaughan,[1,2,22] Emily Wisnioski[2,4] and Sukyoung K. Yi[7]

Affiliations are listed at the end of the paper

Accepted 2023 March 30. Received 2023 March 8; in original form 2022 October 21

ABSTRACT

We investigate the impact of environment on the internal mass distribution of galaxies using the Middle Ages Galaxy Properties with Integral field spectroscopy (MAGPI) survey. We use 2D resolved stellar kinematics to construct Jeans dynamical models for galaxies at mean redshift $z \sim 0.3$, corresponding to a lookback time of 3–4 Gyr. The internal mass distribution for each galaxy is parametrized by the combined mass density slope γ (baryons + dark matter), which is the logarithmic change of density with radius. We use a MAGPI sample of 28 galaxies from low-to-mid density environments and compare to density slopes derived from galaxies in the high density Frontier Fields clusters in the redshift range $0.29 < z < 0.55$, corresponding to a lookback time of ∼5 Gyr. We find a median density slope of $\gamma = -2.22 \pm 0.05$ for the MAGPI sample, which is significantly steeper than the Frontier Fields median slope ($\gamma = -2.00 \pm 0.04$), implying the cluster galaxies are less centrally concentrated in their mass distribution than MAGPI galaxies. We also compare to the distribution of density slopes from galaxies in ATLAS^{3D} at $z \sim 0$, because the sample probes a similar environmental range as MAGPI. The ATLAS^{3D} median total slope is $\gamma = -2.25 \pm 0.02$, consistent with the MAGPI median. Our results indicate environment plays a role in the internal mass distribution of galaxies, with no evolution of the slope in the last 3–4 Gyr. These results are in agreement with the predictions of cosmological simulations.

Key words: galaxies: evolution – galaxies: kinematics and dynamics.

1 INTRODUCTION

The impact of environment on the galaxies they host is an open question in astronomy. The Middle Ages Galaxy Properties with Integral field spectroscopy (MAGPI)[1] has been specifically designed to answer this question. MAGPI is a MUSE/VLT Large Programme survey, aimed at spatially mapping the ionized gas and stellar properties of galaxies in a key transition period in cosmic time. The survey targets 60 massive galaxies around redshift 0.3, and spans field to group environments. In addition to the primary targets, the observed fields contain a wealth of secondary objects across a range of redshifts. In this work, we use this unique data set to begin to untangle what role the large-scale structure surrounding a galaxy plays in shaping its internal mass distribution.

The mass assembly of galaxies is dominated by the collapse and accretion of dark matter, in combination with the accretion of stars and gas at later times, mostly associated with infalling dark matter. The total mass (baryonic and dark matter) distribution can be described as a density profile of the form $\rho(r) \propto r^{\gamma}$, for which γ (< 0) is the total density slope, and indicates how steeply the mass density falls away with radius.

Dynamical modelling has been applied in the local Universe to measure the total density slopes of galaxies, finding a clustering of values around, or just steeper than, $\gamma = -2$ (Thomas et al. 2011; Cappellari et al. 2015; Serra et al. 2016; Poci, Cappellari & McDermid 2017; Bellstedt et al. 2018; Li et al. 2019). These dynamical modelling studies use either the highly general Schwarzschild orbit superposition technique (Schwarzschild 1979) or the simpler Jeans approach (Jeans 1922). The measurement of total density slopes in the Frontier Fields clusters by Derkenne et al. (2021) pushed the Jeans dynamical modelling technique up to redshift 0.55, and found no evidence for the evolution of the slope when comparing to the methodologically consistent study of Poci et al. (2017) in the local Universe. However, indirect observations of dark matter using the rotation curves of star-forming galaxies indicate dark matter haloes were denser at earlier times, suggesting the total profile was correspondingly steeper as well (Sharma, Salucci & van de Ven 2022).

★ E-mail: caro.derkenne@hdr.mq.edu.au

[1]Based on observations obtained at the Very Large Telescope (VLT) of the European Southern Observatory (ESO), Paranal, Chile (ESO programme ID 1104.B-0526).

© 2023 The Author(s)
Published by Oxford University Press on behalf of Royal Astronomical Society

Downloaded from https://academic.oup.com/mnras/article/522/3/3602/7152361 by Universiteit Leiden - LUMC user on 21 February 2024

The technique of gravitational lensing has been applied to observationally determine total density slopes up to redshift ∼0.8. These studies indicate that density slopes are more shallow (less negative) at earlier times than in the local Universe, from ~ -1.7 at $z \sim 0.6$ to slightly steeper than -2 locally (Ruff et al. 2011; Bolton et al. 2012; Li, Shu & Wang 2018). Gravitational lensing requires the most massive of galaxies to act as lenses to the even more distant Universe, perhaps leading to a bias in those samples. Furthermore, dynamical modelling and gravitational lensing techniques make use of different assumptions, and it is unclear what impact these methodological systematics have on the resulting density slope measurements.

Cosmological simulations could provide an effective way to predict the total density slopes and their evolution with redshift. However, only relatively recent simulation suites have been able to achieve this in practice, as a result of their sufficiently high particle resolution. Magneticum is one such suite of simulations. The Magneticum simulations are a set of hydrodynamical simulations with high enough resolution to probe scales within the half-mass radius of galaxies (Dolag 2015). These simulations indicate the average density slope of early-type galaxies was steep in the early universe of value ~ -3 at $z \sim 3$ (Remus et al. 2017). At these early times, galaxy assembly is dominated by gas accretion from cosmic filaments and gas-rich mergers. Both are dissipative processes that result in compact galaxies with high-density central regions. At later times dry mergers dominate, which are particularly effective at increasing the size of the galaxy without a significant increase in mass (Naab, Johansson & Ostriker 2009; Hilz, Naab & Ostriker 2013; Remus et al. 2013), due to their efficient redistribution of mass and angular momentum towards the outskirts of galaxies (Lagos et al. 2018). Consequently, the total density slope is driven from steep to shallower values of $\gamma \sim -2$ in the local Universe, although gas-rich mergers can steepen it again, although such mergers become rare at lower redshifts as the cold gas fraction of galaxies decreases (Remus et al. 2013). Density slopes of $\gamma \approx -2$ are called 'isothermal,' as they correspond to the density slope of a singular isothermal sphere.

There is no consensus on the degree of the evolution of total density slopes across redshift from simulations. The magnetohydrodynamical cosmological simulation set IllustrisTNG (Pillepich et al. 2018) shows little evolution of the total density slope below $z \sim 1$ (Wang et al. 2019). By comparison, Magneticum total density slopes changed from $\gamma \sim -2.3$ to $\gamma sim - 2.0$ between $z = 1$ and $z = 0$. These differences in prediction arise from the specific recipes used in each simulation set, such as gas cooling, stellar winds, and active galactic nucleus (AGN) feedback.

The evolution discussed above does not consider the host environment of a galaxy, which might also impact the internal total mass distribution. In high-density cluster environments, there are numerous processes that can impact galaxy evolution that cannot act on an isolated galaxy in the field. First, ram-pressure stripping acts to strip away the hot gas of galaxies, as they move through the intergalactic medium (Gunn & Gott 1972; Boselli, Fossati & Sun 2022). Secondly, galaxies in clusters have high velocity dispersions and tend to interact frequently at high speed; these encounters, so-called fly-bys and harassments, can tidally distort galaxies in both morphology and kinematics (Moore et al. 1996; Mihos 2003; Bialas et al. 2015; Scott et al. 2018). Lastly, dense environments act to truncate the dark matter haloes of galaxies that have crossed the cluster core compared to galaxies in the field (Limousin et al. 2007, 2009).

Considering only dark matter, a lensing study of 12 early-type galaxies found the density profile of dark haloes may depend on environment, with haloes in high-density environments experiencing expansion due to satellite accretion, and thereby becoming more shallow than dark haloes in less dense environments (Oldham & Auger 2018). Total density slopes have been shown to depend on dark matter fractions both in observations and simulations (Sonnenfeld et al. 2013; Remus et al. 2017). Galaxies with lower dark matter fractions tend to have correspondingly steeper density slopes due to the dominating stellar component within the measurement region. As dark halo properties can vary with environment, we might therefore expect the total density slope to vary as well.

Gas-poor, dry mergers are another key mechanism that can influence the evolution of a galaxy, and are thought to drive the total density slope towards isothermal values (Remus et al. 2013). Using a sample of spectroscopically observed galaxies in the zCOSMOS redshift survey (Lilly et al. 2007), de Ravel et al. (2011) revealed a correlation between local density and merger rates, with major mergers occurring preferentially in high-density regions. Watson et al. (2019) found enhanced merger rates for galaxies in clusters compared to field galaxies at redshift ∼2. This result has also been found by Jian, Lin & Chiueh (2012) in the Millenium simulations (Springel et al. 2005b): they find a strong dependence between merger rates and local overdensities, with galaxies in overdense regions experiencing merger rates up to a factor of 20 greater than those in underdense regions, modulo the semi-analytic model used. Further evidence for increased merger rates in dense environments is the morphology–density relation. Elliptical galaxies are preferentially found in cluster environments, with their transformation from disc to elliptical morphologies caused by merger events (Deeley et al. 2017). From this, we might hypothesize that galaxies in groups and high-density environments have had, on average, more mergers in their history than isolated galaxies of comparable mass, and should therefore have total density slopes closer to isothermal values. In this sense, isothermal total density slopes are indicative low-energy preferential mass distribution (Remus et al. 2013).

Finally, we can look at the dependence of the size–mass distribution of galaxies with environment, as galaxies that are more compact are likely to have steeper total density slopes (Sonnenfeld et al. 2013; Poci et al. 2017; Derkenne et al. 2021). Maltby et al. (2010) used a photometric sample of ∼1200 galaxies across lenticular, spiral, and elliptical morphologies at redshift 0.2, and found no statistically significant dependence of a galaxy's position on the size–(stellar) mass plane with environment, with the exception of some spirals, indicating that internal physical processes dominate over environment in driving size–mass evolution, in agreement with the results of Grützbauch et al. (2011) at redshifts 0.1−0.4. At the extreme end, it is noted that the most massive galaxies are found in correspondingly dense environment (Calvi et al. 2013). In contrast to the above, Cebrián & Trujillo (2014) show galaxies in cluster environments tend to be slightly more compact than their field counterparts.

To begin to answer the complex question of the relation between total mass density slopes and environment, we present Jeans dynamical modelling results and total density slopes of 30 galaxies from the MAGPI survey. Out of these 30, we present a total density slope analysis for 28 galaxies. We use 2D, resolved stellar kinematic maps to constrain the total gravitational potential with Jeans anisotropic models. This sample of galaxies is drawn from a mix of field and group environments, less extreme and less dense than the Frontier Fields clusters studied by Derkenne et al. (2021), and roughly comparable in environment to the local sample of ATLAS^{3D} galaxies modelled by Poci et al. (2017). We compare to these two other studies in particular, as they both used an identical modelling technique and definition of the total potential to what we implement in this work,

Downloaded from https://academic.oup.com/mnras/article/522/3/3602/7152361 by Universiteit Leiden - LUMC user on 21 February 2024

and their inclusion allows us to span environments: field galaxies, groups, and clusters.

By using a combined sample from studies that use a consistent methodology, we can determine what impact the broad categorization of environment has on the total density slope, and investigate whether there has been any evolution in the total density slope between the MAGPI and Frontier Fields samples in the 'middle ages' compared to the ATLAS^{3D} sample in the local Universe. When the full MAGPI sample is observed we intend to use finer environmental metrics for analysis purposes. We also compare our observational results to the simulation predictions from the Magneticum, IllustrisTNG, and Horizon-AGN simulations (Dubois et al. 2014).

Section 2 describes the MAGPI survey data, sample selection, and data-quality cuts made in this work. Section 2 also outlines all other data sets used for comparison in this work. Section 3 describes the measurement of the stellar kinematics, stellar potentials, Jeans model definitions, and the calculation of the total density slope. The results are presented in Section 4, with a discussion following in Section 5. Conclusions are given in Section 6.

Throughout this article, we use a flat ΛCDM cosmology with $H_0 = 70$ km s^{-1}Mpc^{-1} and $\Omega_m = 0.3$. All scales are converted (angular and physical units) using the angular diameter distance given by the object's redshift and the above cosmology. At the nominal redshift of the MAGPI survey, $z \sim 0.3$, this results in ∼4.45 kpc per arcsecond. For comparison, a galaxy only 40 Mpc distant (local, and approximately the distance of galaxies in the ATLAS^{3D} comparison sample) has a scale factor of ∼0.19 kpc per arcsecond.

2 DATA

In this section, we give an overview of the MAGPI data we use to derive total density slopes, and the two main comparison data sets of ATLAS^{3D} and Frontier Fields. We follow with a description other literature data sets and cosmological simulations we compare to.

2.1 MAGPI

This work uses the first tranche of observed data from the MAGPI[2] survey (the 16 fields observed before August 2021 of the 56 total fields to be observed). MAGPI is a VLT/MUSE Large Programme still gathering observations at the time of writing (PIs: Foster, Harborne, Lagos, Mendel, and Wisnioski). The survey targets 60 primary galaxies at $z \sim 0.3$ with stellar masses estimated at $M_\star > 7 \times 10^{10}$ M$_\odot$. Primary targets were selected from the GAMA survey, chosen so that the final MAGPI sample spans environments from isolated galaxies to galaxies in groups. The fields we present here are representative of the full sample. Two archival cluster data sets act as high-density environment supplements: clusters Abell 2744 at $z = 0.308$ and Abell 370 at $z = 0.375$ (programme ID 096.A-0710, PI: Bauer and programme IDs 095.A-0181 and 096.A-0496, PI: Richard, respectively). The survey aims and description are presented in full by Foster et al. (2021). Briefly, the survey aims to map stellar and ionized gas components of galaxies in the relatively unobserved 'middle ages' of the Universe, with comparable relative spatial resolution to local Universe studies like the Sydney-Australian-Astronomical-Observatory Multi-object Integral-Field Spectrograph (SAMI) survey (Croom et al. 2012), and Mapping Nearby Galaxies at Apache Point Observatory (MaNGA; Bundy et al. 2015) survey. These observations will provide the key to unlocking the role of environment and assessing the impacts of merging, metal mixing, and energy sources in galaxies at this time. The survey includes foreground and background objects, extending the redshift baseline the survey can probe.

[2]https://magpisurvey.org

Table 1. Column 1 lists the MAGPI fields used in this work, with galaxies selected based on data-quality cuts outlined in Appendix A. Column 2 lists the PSF FWHM in arcseconds, as measured from an MGE of a stack of point sources in each field in the SDSS *r*-band, described in Section 3.1.

Field	PSF FWHM (arcsec)
1202	0.70
1203	0.63
1204	0.78
1205	0.67
1206	0.71
1207	0.62
1208	0.74
1209	0.59
1501	0.65
1507	0.59
1508	0.57
1523	0.59
1525	0.63
1530	0.69

The programme uses MUSE in the wide-field mode with the nominal wavelength range, resulting in spectra in the range 4650–9300 Å in steps of 1.25 Å per pixel. A ground-layer adaptive optics (GLAO) system is used to reduce the impact of seeing on the observations, resulting in a gap in wavelength coverage from 5780–6050 Å due to the GALACSI system sodium laser notch filter (Hartke et al. 2020). The point spread function (PSF) full width at half-maximum (FWHM) is indicated for each field used in this work in Table 1. The MAGPI fields cover a 1 × 1 arcmin field of view with 0.2 arcsec per pixel spatial sampling. Each field is observed across six observing blocks of 2 × 1230 s exposures, resulting in a total on-source integration time of 4.4 h per field (246 h on-source total).

The data reduction process will be described in detail in an upcoming paper (Mendel et al. in preparation), but here we provide a brief overview. Reduction was based on the MUSE reduction pipeline (Weilbacher et al. 2020), with sky-subtraction completed using Zurich Atmosphere Purge sky-subtraction software (Soto et al. 2016). All fields have segmentation maps and estimates of galaxy structural parameters, such as the effective radius created using ProFound (Robotham et al. 2018). Each source identified within a field is post-processed to be situated at the centre of a 'minicube' based on the main MUSE cube, which is sized to encompass the maximum extent of the 'dilated' segmentation map determined by ProFound. An example of the richness of the MAGPI fields is shown in Fig. 1.

At present, the highest resolution and deepest imaging data for MAGPI galaxies are the MUSE observations themselves. Mock images are created from the MUSE cube for each field in the SDSS $g_{\rm mod}$, r, i, and $z_{\rm mod}$ bands based on the mean flux density within the filter region. The g and z bands are only partially covered by MUSE, and are so labelled 'mod(ified)'.

We investigated the impact of creating multi-Gaussian expansions (MGEs) of the stellar light based on MUSE cubes with detailed, end-to-end simulations (see Appendix A). The potential issue is that poorly resolved galaxies will have a modelled light distribution which is less centrally peaked than it should be, resulting in a bias towards

Downloaded from https://academic.oup.com/mnras/article/522/3/3602/7152361 by Universiteit Leiden - LUMC user on 21 February 2024

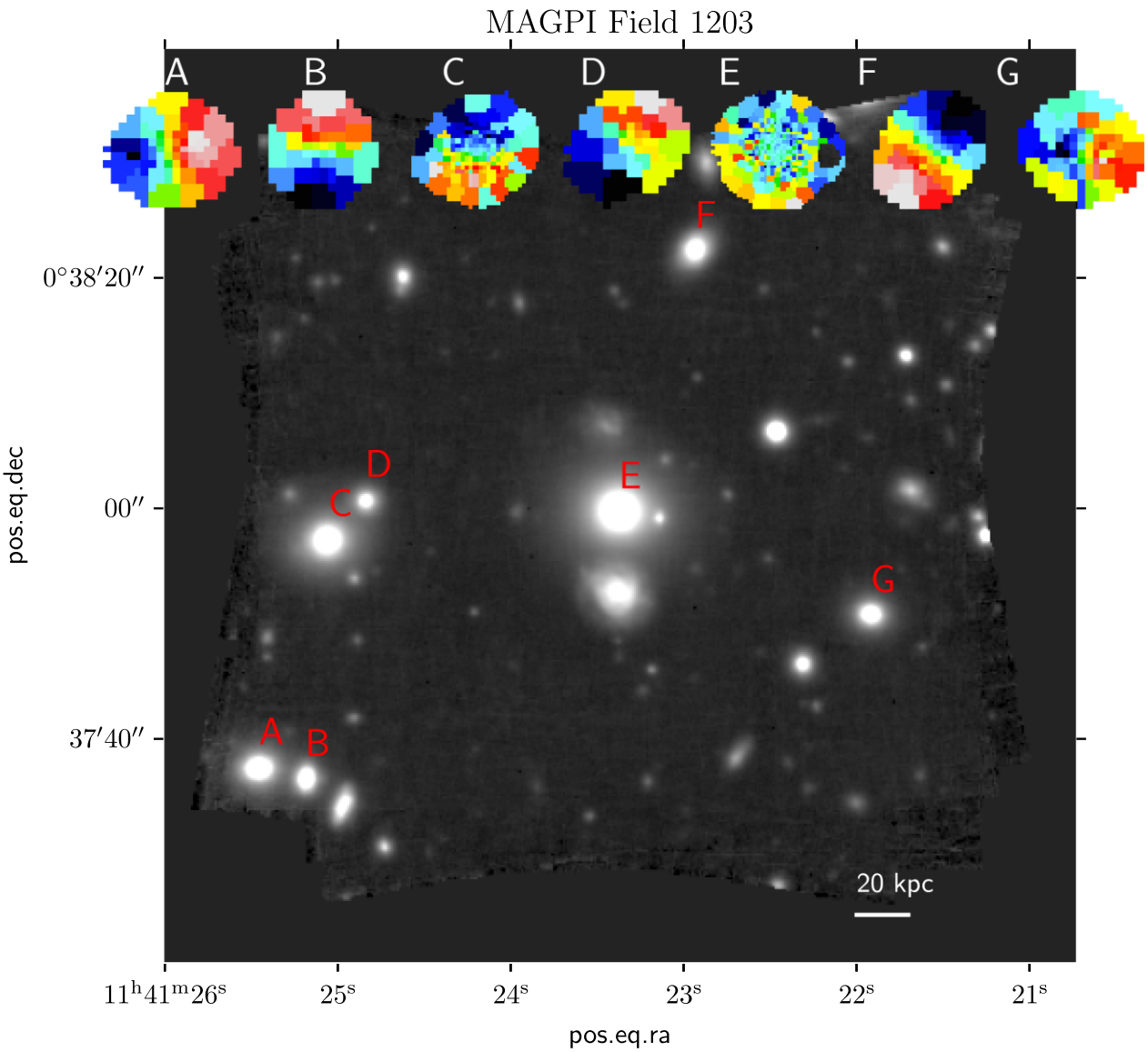

Figure 1. MAGPI field 1203 as an equivalent *r*-band image extracted from the MUSE data cube by summing over a broad spectral band in the wavelength direction. Field 1203 is the richest field used in this work in terms of number of galaxies that meet the data quality requirements for measuring a total density slope. A 20 kpc scale at $z = 0.3$ is inset. The letter labels indicate which inset velocity field match which object in the field. These fields are indicative only, and are not to scale spatially. Object E is the central target. The MAGPI IDs are as follows: A = 1203040085, B = 1203060081, C = 1203070184, D = 1203087201, E = 1203196196, F = 1203230310, G = 1203305151.

more shallow total density profiles. Our simulations show poorly resolved galaxies with multiple effective radii of kinematic coverage bias slopes towards steeper values, whereas resolved galaxies with less than an effective radius of kinematic coverage bias slopes to more shallow values. We determine there is no inherent bias in the recovered parameters using MUSE-based MGEs, so long as modelled galaxies have elliptical effective radii (R_e) greater than or equal to the PSF FWHM, and stellar kinematics extend up to at least $1.5R_e$. We applied these cuts to the sample, giving a sample of 30/72 MAGPI galaxies from 14/16 fields. Further cuts based on analysis and not data quality, outlined in Section 3.4, adjust the final sample used to calculate the median total density slope value as 28 MAGPI galaxies.

Fig. 2 shows the thumbnails of all MAGPI fields analysed to create the final sample of galaxies used in this work.

2.2 Main comparison data sets: ATLAS^{3D} and Frontier Fields

We compare the MAGPI total density slopes to two main observational samples. The first is the Frontier Fields (Lotz et al. 2017) sample of galaxies, modelled in Derkenne et al. (2021). These modelled galaxies are drawn from the five Frontier Fields clusters that have optical integral field unit (IFU) data; Abell 2744, Abell 370, Abell S1063, MACS J0416.1−2403, and MACS J1149.5+223. These clusters were chosen as part of the Frontier Fields programme for the likelihood of having a high number of gravitational lensing systems, and so necessarily represent very dense galaxy environments. The clusters have MUSE/VLT data cubes and *Hubble Space Telescope* (*HST*) data, and span $0.29 < z < 0.55$. The sample as modelled in Derkenne et al. (2021) is 90 early-type galaxies.

The second comparison sample are the 260 ATLAS^{3D} galaxies (Cappellari et al. 2011), a volume-limited sample of galaxies in the

Downloaded from https://academic.oup.com/mnras/article/522/3/3602/7152361 by Universiteit Leiden - LUMC user on 21 February 2024

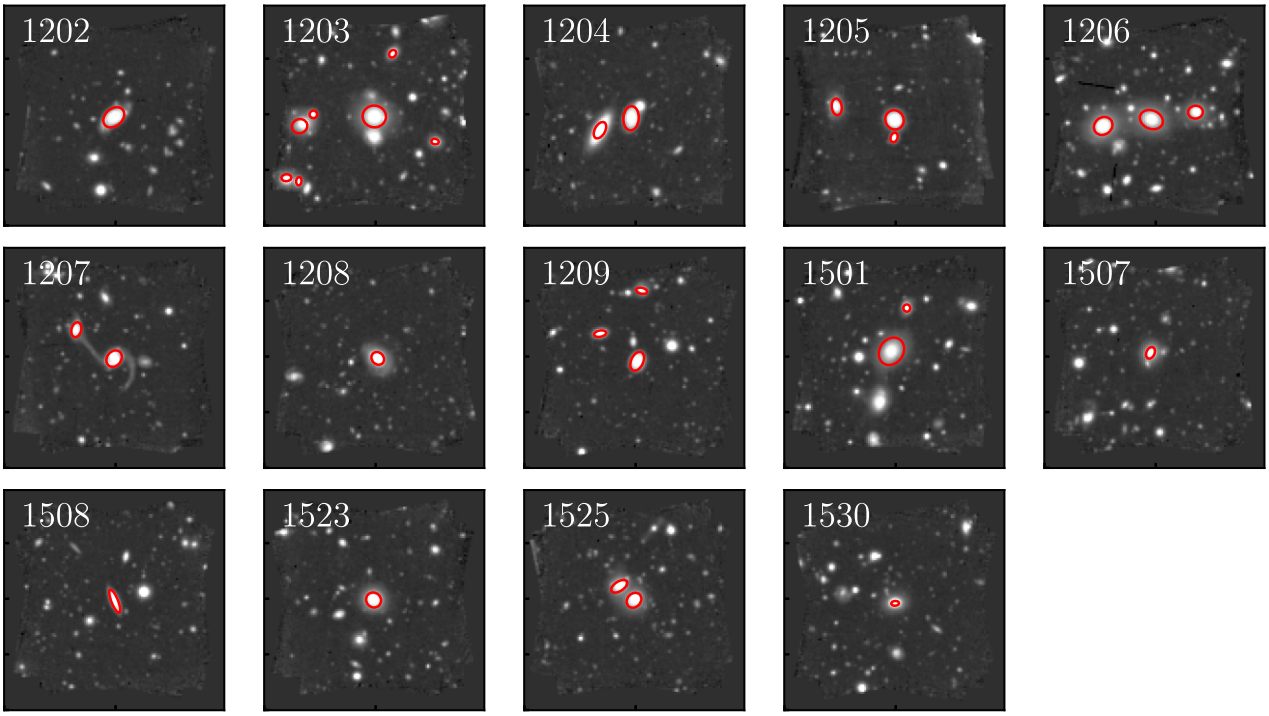

Figure 2. All the MAGPI SDSS *r*-band images of fields used in this study. This is a subset (14/16) of the available MAGPI fields at the time of writing due to data quality cuts on the sample (see Section 2). Inset on each image is the MAGPI field name. Red ellipses show all the MAGPI objects used in this work; the ellipses have major-axis equal to twice the major-axis from the PSF-deconvolved MGEs for visibility.

local Universe. Objects were selected to be closer than 42 Mpc with a magnitude limit of $M_K < -21.5$ mag. IFU data were collected by the SAURON integral-field spectrograph mounted on the William Herschel Telescope on La Palma. Optical data were gathered using the Wide-Field Camera at the 2.5m Isaac Newton Telescope, if imaging did not already exist as part of the *Sloan Digital Sky Survey* (SDSS). Poci et al. (2017) used Jeans dynamical models to constrain the total gravitational potential for 258 of these galaxies (Model 1 in that work). In this work, we only include ATLAS^{3D} galaxies for analysis that have a data quality flag $\geq$1 as defined in Cappellari et al. (2013a) (187/258 galaxies). The dynamical models of Derkenne et al. (2021) and Poci et al. (2017) use the same formulation of the total gravitational potential.

2.3 SLUGGS and Coma

Thomas et al. (2011) constructed Schwarzschild dynamical models of 17 galaxies in the Coma cluster, a massive cluster in the local Universe ($z = 0.0231$), in order to constrain their luminous and dark matter distributions. The models assumed separate luminous (from an MGE) and dark matter (a Navarro–Frenk–White halo) components to form the total density profile, whereas in this work we use a single profile to describe the total density profile. Models were constructed using the orbit superposition technique of Schwarzschild modelling (Schwarzschild 1979). The dynamical models of Thomas et al. (2011) provide a valuable data set of total density profiles measured in a massive cluster environment in the local Universe. We use the total density profiles as constrained by the models presented in Thomas et al. (2011), but re-calculate the total density slope within the radial range $r = [R_e/10, 2\,R_e]$ to match that used for MAGPI, Frontier Fields, and ATLAS^{3D} galaxies (see Section 3.4).

Another local sample of galaxies with constrained total density profiles from dynamical models are the SLUGGS (SAGES Legacy Unifying Globulars and GalaxieS Survey) galaxies, as presented by Bellstedt et al. (2018). Globular cluster kinematics at large radii were combined with stellar kinematics from ATLAS^{3D} data at small radii for 22 galaxies. Many modelling choices for the SLUGGS sample overlap with the modelling approach in this work; a double power-law potential was used to describe the total gravitational potential with a fixed transition between a free inner slope and constant outer density slope at 20 kpc (see Section 3.3 for the Jeans model descriptions used in this work). However, a hyperparameter was used to independently weight the globular cluster data and stellar kinematics in order to fit the combined $v_{\rm rms}$ fields. It is as of yet unclear what systematics this introduces compared to a method that uses stellar IFU data alone. For comparisons, we use the most likely parameters from the EMCEE posterior distributions from the models as given by Bellstedt et al. (2018). As with the Coma data, we re-calculate the SLUGGS total density slopes within the radial range of $r = [R_e/10, 2\,R_e]$.

2.4 Simulations: Horizon-AGN, Magneticum, and IllustrisTNG

The first simulation comparison sample we use comes from the Horizon–AGN simulation. The Horizon-AGN simulation uses the adaptive mesh refinement code RAMSES (Teyssier 2002) and has a co-moving volume of $(100\ {\rm Mpc}\,h^{-1})^3$ with a dark matter particle resolution of $m_{\rm DM} = 8 \times 10^7\ {\rm M}_\odot$. The simulations incorporates gas cooling, stellar winds from STARBURST99 (Leitherer et al. 1999), and AGN feedback following Dubois et al. (2012).

We present Horizon-AGN simulation total density slopes calculated in the radial range $r = [R_e/10, 2\,R_e]$ with a single power-law fit, to closely match the method used to measure total density slopes for

Downloaded from https://academic.oup.com/mnras/article/522/3/3602/7152361 by Universiteit Leiden - LUMC user on 21 February 2024

MAGPI galaxies from the total density profile. The Horizon-AGN sample presented here is comprised of galaxies from 14 simulation snapshots spanning $0.018 < z < 0.305$, with stellar masses between 10^{11} and 10^{12} $M_\odot$. Because of gravitational softening within the simulations, no region within a physical scale of 2 kpc is used to fit the total density slope, although we do not expect this choice to drive the observed trends. The median value of $1R_e$ for the Horizon-AGN sample is 1 kpc, which is smaller than the 2 kpc bound imposed. However, the single power-law density slope is not particularly sensitive to these innermost regions of simulated galaxies.

The second simulation data set we use for comparisons are the published total density slopes from the Magneticum Pathfinder simulations as calculated by Remus et al. (2017). For that work, the cosmological box volume is $(48\ \mathrm{Mpc}\,h^{-1})^3$, with a dark matter particle resolution of $m_{\rm DM} = 3.6 \times 10^7 \mathrm{M}_\odot\, h^{-1}$. To avoid the effects of softening and resolution, total density slopes are calculated on the radial range of $0.4-4\ R^{\rm 3D}_{1/2}$, where $R^{\rm 3D}_{1/2}$ indicates the 3D half-mass radius. As an additional criteria, if $0.4R_e$ is smaller than twice the gravitational softening length, then twice the softening length is adopted as the inner radial bound. This change of bound only occurs for very few galaxies. The simulations are run with smoothed particle hydrodynamics in the form of the GADGET3 code (Hirschmann et al. 2014), and include gas cooling, passive magnetic fields, and AGN feedback (Springel & Hernquist 2003; Springel, Di Matteo & Hernquist 2005a; Fabjan et al. 2010). The studied galaxies have stellar masses greater than $M_\star = 5 \times 10^{10}$ $M_\odot$.

Finally, we also compare to slopes calculated by Wang et al. (2019) using galaxies in the IllustrisTNG simulations. The particular cosmological box volume used in that work is $(110.7\ \mathrm{Mpc}\,h^{-1})^3$ with a dark matter particle resolution of $m_{\rm DM} = 7.5 \times 10^6$ $M_\odot$. IllustrisTNG uses the adaptive moving-mesh code AREPO (Springel 2010). Stellar and AGN feedback follows the prescriptions of Pillepich et al. (2018) and Weinberger et al. (2018). The published slopes of Wang et al. (2019) are calculated using the range $0.4-4R^{\rm 3D}_{1/2}$, the inner bound again set to avoid gravitational softening effects. The sample includes early-type galaxies with stellar masses concentrated within an aperture of 30 kpc between $M_\star = 10^{10.7}$ $M_\odot$ and $M_\star = 10^{11.9}$ $M_\odot$.

We stress that the implementations of gas physics and feedback are different in these simulations, and these differences will necessarily impact the internal mass distribution of simulated galaxies. For example, the exact implementation of gas cooling in the simulations can lead to differences in the mass distribution, as cooling can cause star formation at later times and increase galaxy central densities.

2.5 Other literature data sets

We collate several other literature data sets against which we compare our results. First, Li et al. (2019) constructed Jeans models for a sample of 2110 nearby galaxies from the MaNGA survey. Second are density slopes measured using galaxies from the Sloan Lens ACS (SLACS) survey (Bolton et al. 2006), published in Auger et al. (2010) and Barnabè et al. (2011), and based on gravitational lensing techniques. Thirdly, we compare to density slopes presented in Bolton et al. (2012), which combined strong gravitational lensing with a dynamical analysis to measure total density slopes, utilizing data from SLACS and the BOSS Emission Line Lensing Survey (BELLS). Fourth are the density slopes from the Strong Lenses in the Legacy Survey (SL2S), as published by Ruff et al. (2011) and Sonnenfeld et al. (2013). Finally, we compare to density slopes derived from a combined analysis of BELLS and BELLS GALaxy-Ly α EmitteR sYstems (GALLERY) Survey, and SL2S galaxies, as published in Li et al. (2018), again using a strong gravitational lensing technique.

3 METHODS

3.1 Multi-Gaussian expansion of stellar light

The stellar light distribution is parametrized as a series of 2D Gaussians, to be used as input to the Jeans dynamical models as the luminous tracer. An assumed viewing angle de-projects the observed surface brightness to a 3D luminosity density (Emsellem, Monnet & Bacon 1994). Here, we use the PYTHON package MGEFIT to fit the stellar light (Cappellari 2002). MGEs were fit to SDSS r-band, chosen for image depth.

Sources other than the target galaxy were masked using the PROFOUND (Robotham et al. 2018) segmentation maps. The initial fit area was cut as a square of sides $20R_e$ (from MAGPI data PROFOUND outputs, as described in Foster et al. 2021) to ensure the fit was not artificially contracted, as this thumbnail size includes sky-dominated boundaries. The threshold level of the fit was determined by the median of the set of pixels associated with no source according to the segmentation maps.

A regularized fit was performed on the r-band mock images, meaning the roundest possible solution was found with the least number of Gaussian components that did not perturb the absolute deviation of the model excessively far from the best-fit model (here we allow for a 3 per cent deviation, empirically determined). Regularization allows for the largest possible range of galaxy inclinations, still consistent with the data, to be tested in the subsequent Jeans models.

MGE models of the PSF were made using stacked point sources in each of the MAGPI fields. The MGE surface brightness model of each galaxy was then analytically convolved with the corresponding PSF and the fit optimized against the observed galaxy surface brightness (Cappellari 2002). This optimized, underlying MGE surface brightness model with no PSF convolution was used as the luminous tracer in the Jeans models described in Section 3.3.

This work uses Jeans models with a total potential that sets the scaling of the gravitational potential, meaning the scaling of the luminous component is irrelevant; only the relative scaling, widths, and shapes of the luminous Gaussians impact results. For each galaxy, N 2D Gaussian components are used to describe the light, consisting of the total image counts enclosed by the $N^{\rm th}$ Gaussian in the image units, its sigma-width in pixels (σ), and the observed axial ratio of the Gaussian (q). To prepare the MGEs as inputs to the Jeans models the Gaussian enclosed counts (C) in image units were re-normalized to a peak surface brightness (C_0) for each of the N components:

$$C_0 = \frac{C}{2\pi\sigma^2 q}. \tag{1}$$

The Gaussian dispersions were converted from pixel to observed units by multiplying by the image pixel scale. An example MGE model for a MAGPI galaxy is shown in Fig. 3.

At this point, galaxies with very poorly fitting MGEs (as judged by visual inspection) were excluded from the sample. This exclusion is mainly restricted to galaxies with high elliptical shapes but small effective radii where the PSF-deconvolution could not be accurately performed and the resulting model bore little resemblance to the galaxy's light distribution. This means we exclude some small, highly flattened systems. Our final sample spans up to 0.73 in ellipticity, with a mean ellipticity of 0.26; this distribution is comparable to the ATLAS$^{\rm 3D}$ survey (Emsellem et al. 2011).

Downloaded from https://academic.oup.com/mnras/article/522/3/3602/7152361 by Universiteit Leiden - LUMC user on 21 February 2024

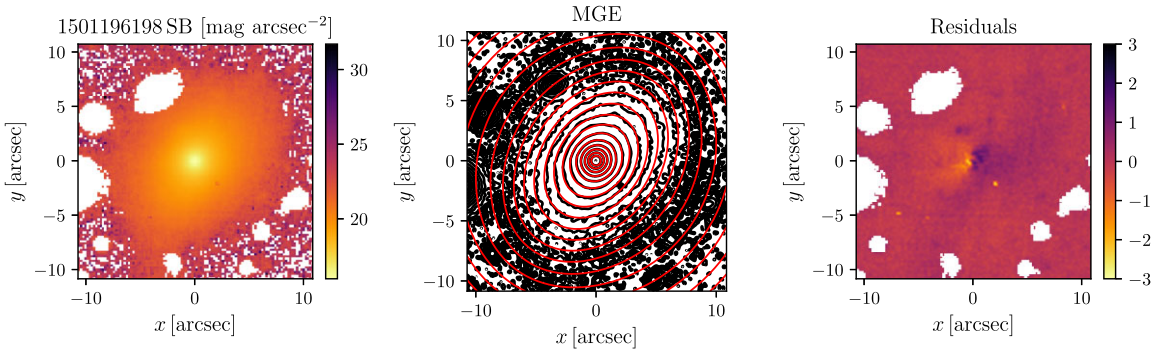

Figure 3. Left: The SDSS r-band surface brightness of MAGPI object 1501196198 in the STMAG magnitude system (Stone 1996). The white regions show masked pixels due to neighbouring galaxies. These pixels were excluded from the subsequent fit. Middle: The PSF-convolved MGE model in red, over plotted on the black galaxy isophotes, in steps of 0.5 mag per square-arcsecond. The MGE contours mostly cover the image contours. Right: The residuals (data – MGE model) divided by the noise of the flux image.

The effective radius was derived as the circularized arcsecond extent which contains half the measured light of the galaxy. These radii are used in all subsequent analysis, and are provided in Table C1.

3.2 2D stellar kinematics

Full-spectrum fitting using the PYTHON package PPXF was used to derive the stellar kinematic fields (Cappellari & Emsellem 2004; Cappellari 2017). In this work, we set the higher order Hermite coefficients (h3 and h4) to zero which ensures the line-of-sight velocity distribution is described by a Gaussian. From the velocity and velocity dispersion fields, the $v_{\rm rms}$ field is constructed as $v_{\rm rms}=\sqrt{v^2+\sigma^2}$.

We used the Indo-US template library (Valdes et al. 2004) as it has a sufficiently high spectral resolution of 1.35 Å FWHM so that the stellar templates could be convolved with a Gaussian kernel to match the mean spectral resolution within the spectral window used (for MUSE this is ~ 2.5 Å, Mentz et al. 2016).

The minicube of each MAGPI source was thresholded to a signal-to-noise ratio of 1.5 per pixel in the fitted spectral region, which is approximately 3500–6500 Å in rest frame but depends on the redshift of each galaxy. Each galaxy was Voronoi binned to a signal-to-noise ratio of 10 per spectral pixel per bin using the PYTHON package VORBIN (Cappellari & Copin 2003). The binning ensures a high enough signal to noise across the field to recover kinematics without excessively truncating the radial coverage. It is also exactly matched to the binning process used by Derkenne et al. (2021), which ensures the resulting dynamical models can be fairly compared against that work.

We restricted the range of Indo-US templates for each spectrum fit by first using the MGE model parameters (effective radius, ellipticity) to create an elliptical $1R_{\rm e}$ co-added spectrum. This central spectrum was fitted with the entire Indo-US template library, after which the template library for the spectral fit of each individual bin was limited to the top-weighted 20 template spectra of the central fit. In detail, a fifth-order multiplicative polynomial was used in the fit, with no additive polynomials.

Uncertainties on the fitted velocity and velocity dispersions were estimated by randomly shuffling the residuals between the observed spectrum and the best-fit spectrum and adding them back on to the observed spectrum in a Monte-Carlo process across 100 iterations. Resulting uncertainties were reduced by $\sqrt{2}$ to account for the doubling of the noise this process involved. An observed spectrum in the rest-frame, the best-fitting determined by PPXF, and the kinematic fields with associated errors are shown in Fig. 4. At this point in the analysis, galaxies with contaminated kinematics due to a projected or actual neighbour were removed upon visual inspection (two objects).

3.3 Jeans modelling

We use Jeans anisotropic models (JAM) created using the PYTHON package JAMPY to constrain the total gravitational potential (Cappellari 2008). Following the JAMPY method, a galaxy is a large system of stars, the velocities and positions of which can be described using a distribution function. If we assume the system is in a steady state with a smooth gravitational potential, then the distribution function must obey the collisionless Boltzmann equation. However, this equation has infinite solutions, which necessitates further assumptions. To achieve a unique solution, the gravitational potential is assumed to be axisymmetric, and in the implementation of JAMPY used here it is assumed that the velocity ellipsoid is aligned with the cylindrical coordinate system. The velocity ellipsoid is the 3D distribution of velocity dispersions in the radial, azimuthal, and z directions, where z is along the axis of symmetry. Aligning the velocity ellipsoid with cylindrical coordinates is observationally motivated by the fact that anisotropy in galaxies can be well characterized as a flattening of the velocity ellipsoid in the z direction (Cappellari et al. 2007). In JAM, the global anisotropy term is defined as

$$\beta_z \equiv 1-\left(\frac{\sigma_z}{\sigma_R}\right)^2, \tag{2}$$

where R denotes the radial direction. The inclusion of this terms allows deviations from perfectly isotropic orbital structures.

These assumptions yield the general axisymmetric, anisotropic Jeans equations, given in equations (8) and (9) in Cappellari (2008). An assumed inclination, anisotropy, and gravitational potential is used to predict the root mean square velocity, defined as $v_{\rm rms}=\sqrt{v^2+\sigma^2}$. The observed velocity and velocity dispersions fields from Section 3.2 were combined into a single measurement per Voronoi bin. The weighting of each bin in the models was determined by use of the error vector

$$\delta v_{\rm rms}=\frac{\sqrt{(v\delta v)^2+(\sigma\delta\sigma)^2}}{v_{\rm rms}}. \tag{3}$$

The JAM model predictions are analytically convolved with the circular PSF of each field (see Table 1) before comparison to the observed $v_{\rm rms}$ field. In this sense, the optimized $v_{\rm rms}$ field is PSF deconvolved, and the constrained total density profile should be

Downloaded from https://academic.oup.com/mnras/article/522/3/3602/7152361 by Universiteit Leiden - LUMC user on 21 February 2024

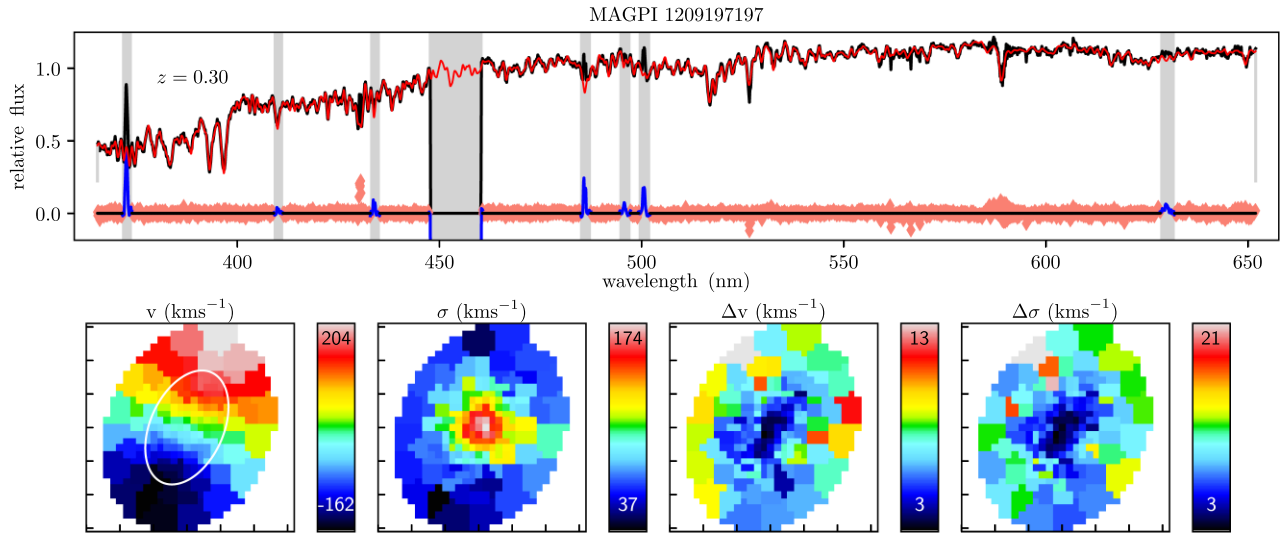

Figure 4. Top row: The full-spectrum fit of MAGPI galaxy 1209197197. The spectrum is shown in black, and is the co-added spectra within an elliptical aperture with semimajor axis equal to $1R_e$. The best fit to the central spectrum is shown in red, with excluded regions shown in grey (including the notch filter from the GALACSI laser band). Blue indicates masked ionized gas emission. The residuals from the fit are shown in pink. The spectral fit was made using PPXF (Cappellari & Emsellem 2004; Cappellari 2017). Bottom row: The extracted velocity, velocity dispersion, 1σ uncertainty on the velocity, and 1σ uncertainty on the velocity dispersion. A white ellipse on the velocity panel shows $1R_e$. The *x*- and *y*-axis ticks are 1 arcsec intervals.

likewise independent of the PSF. The model quality is judged against the observed $v_{\rm rms}$ field using a χ^2 statistic, taking each Voronoi bin as a degree of freedom.

In our models, the total gravitational potential (baryons and dark matter) is described as a spherical double power law of the form

$$\rho(r) = \rho_s \left(\frac{r}{r_s}\right)^{\gamma'} \left(\frac{1}{2} + \frac{1}{2}\frac{r}{r_s}\right)^{-\gamma'-3}, \tag{4}$$

where ρ is the total density as a function of galactocentric radius, γ' is the *inner* density slope, r_s is the 'break' radius at which the potential changes from a free inner slope to a fixed logarithmic outer slope of -3, fixed at 20 kpc, and ρ_s is the density of the total profile at radius r_s. This profile is a 'Nuker' profile, a type of generalized Navarro–Frenk–White (NFW) profile (Lauer et al. 1995; Navarro, Frenk & White 1997). This profile is input to the models as a 1D MGE. The total density slope γ is calculated from this profile once the parameters have been fit to the observed data, discussed in Section 3.4, and is the defined as

$$\gamma = \frac{\mathrm{d}\log(\rho)}{\mathrm{d}\log(r)}. \tag{5}$$

The formulation of the total potential given in equation (4) allows for a luminous component in the inner regions of the galaxy (as traced by the luminous MGE described in Section 3.1) situated within a dark matter halo. We implement a spherical potential and use a fixed break radius of 20 kpc to be consistent with the dynamical models of Poci et al. (2017) and Derkenne et al. (2021). We explore the impact of this choice of break radius in Appendix B.

Furthermore, Poci et al. (2017) found that considering a non-spherical halo did not change the total density slope values or result in improved models. Bellstedt et al. (2018) found that a variable break radius could not be well constrained by the data, despite the large radial coverage of SLUGGS (Brodie et al. 2014) data. When the break radius was left free, Bellstedt et al. (2018) found that the derived total density slopes were consistent (within error) with those found using a 20 kpc fixed break radius.

In our definition of the total potential, there are four free parameters:

(i) The inner density slope γ', bounded between -3.5 and 0.5.

(ii) The log density at the break radius ρ_s, bounded by -4 and 0 with ρ in units of $\mathrm{M}_\odot\ \mathrm{pc}^{-3}$.

(iii) The inclination of the galaxy i, used to de-project the observed luminous surface density. The maximum inclination allowed is 90 deg (edge on). The minimum inclination is set as $i = \cos^{-1} q$, where q is the smallest observed axial ratio from the luminous MGE fit.

(iv) The global anisotropy β_z, which accounts for the flattening of the velocity ellipsoid in the z direction, bounded by -0.5 and 0.5.

To estimate the parameter posterior distributions the PYTHON package EMCEE (Foreman-Mackey et al. 2013; Hogg & Foreman-Mackey 2018) was used, with hundreds of thousands of independent model evaluations made to estimate the posterior distribution for each free parameter. We used 30 independent walkers with a maximum of 10 000 steps, although chains could terminate in fewer steps if the deemed converged by autocorrelation time estimates. The χ^2 statistic of the observed and modelled $v_{\rm rms}$ fields were used to estimate the likelihood of any particular model. Flat (uniform) priors were assumed, that is, the likelihood of a particular model was informed *only* by the χ^2 statistic. Fig. 5 shows a set of Jeans models around the median model from the posterior distribution to visualize the EMCEE process and associated uncertainties.

Fig. 6 shows the estimated marginalized posterior distributions for each of the four free parameters in the Jeans models, with the $v_{\rm rms}$ field constructed from the median of the posterior distributions inset. None of the galaxies in our sample have best-fitting values of the inner total density slope on the boundaries of the original prior. This indicates that the constraints for the parameter chains are data-driven, not prior-driven.

Although the fixed break radius of 20 kpc is outside the kinematic coverage for all but two of the galaxies in the MAGPI sample, the density at this radius is still well constrained. This is due to the fact that the density at the break radius affects the enclosed mass, and

Downloaded from https://academic.oup.com/mnras/article/522/3/3602/7152361 by Universiteit Leiden - LUMC user on 21 February 2024

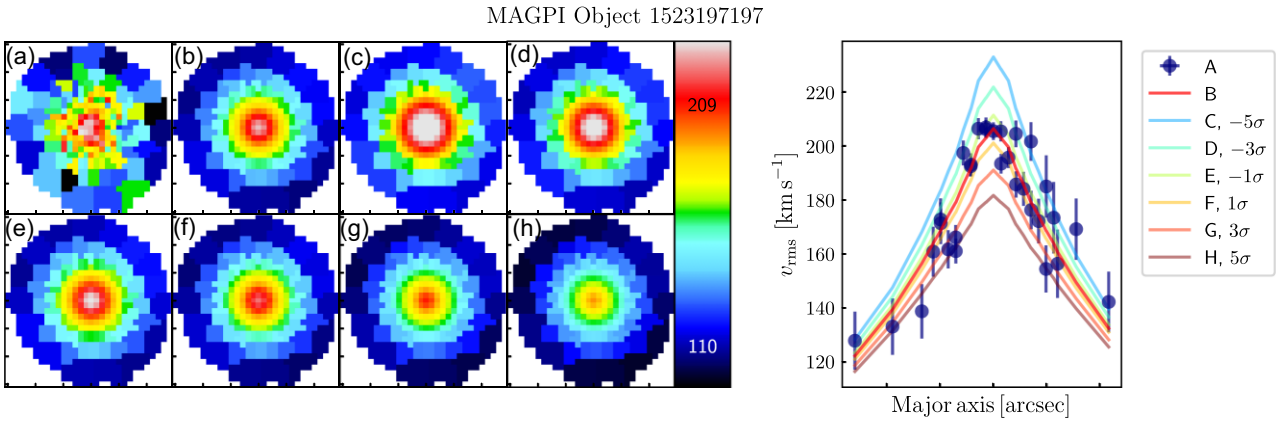

Figure 5. Top row (Panel A): The observed $v_{\rm rms}$ field for MAGPI galaxy 1523197197. Panel B: The median JAM model from the posterior distributions of the EMCEE process. Panels C-H: The resulting $v_{\rm rms}$ field at ± 1, 3, 5σ in γ' around the median solution to illustrate the changes in structure and scale of the $v_{\rm rms}$ field. The *x*- and *y*-axis ticks are 1 arcsec intervals. The total density slope and 1σ uncertainty for this object is $\gamma = -2.28^{+0.01}_{-0.01}$. Right: A $v_{\rm rms}$ major axis cut of the models and observed data, corresponding to the fields shown in Panel A. The $v_{\rm rms}$ errors are shown for the observed data (A).

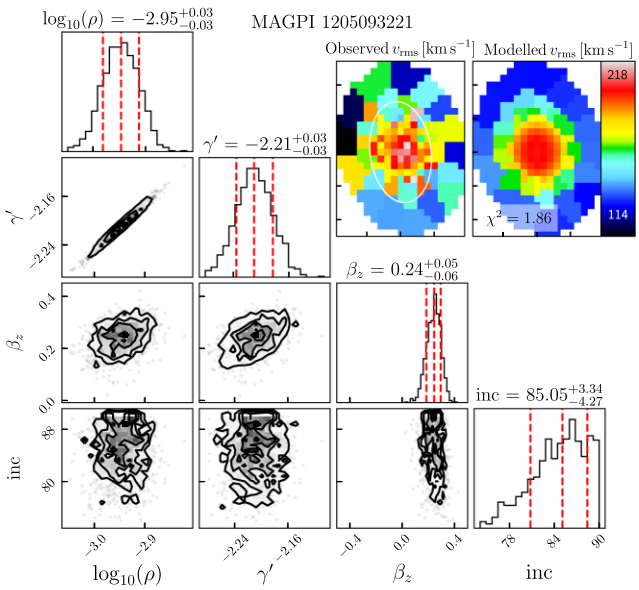

Figure 6. An example corner plot from the EMCEE process for MAGPI object 205093221, with the 16th, 50th, and 84th percentiles of each posterior distribution shown as red dashed lines. Diagonal panels show estimates of the posterior probability distributions, marginalized over one parameter. Off-diagonal panels show the estimated posterior distribution marginalized over every pair of parameter in 2D. In general, there is some covariance between $\rho_{\rm s}$ and γ', as evidenced by the ellipsoidal 2D estimated posterior distribution for those parameters. This covariance is due to both parameters affecting the enclosed mass of the model. Left: The observed $v_{\rm rms}$ field with $1R_{\rm e}$ shown as a white ellipse. Right: The $v_{\rm rms}$ model corresponding to the median of the posterior distributions. The reduced χ^2 value is also given. The *x*- and *y*-axis ticks are 1 arcsec intervals.

therefore the level of the $v_{\rm rms}$ field, for all radial positions interior to the break radius where kinematic data does exist.

3.4 Calculation of the total slope γ

A double power law is used in this work, which includes a smooth transition between inner and outer regimes at a fixed transition radius of 20 kpc. The slope (equation 5) itself is measured as a single power-law fit across some radial range. The specific radial range over which an average total density slope is measured will therefore have an impact on the result. We argue it is crucial to compare the MAGPI sample and main comparison samples, ATLAS$^{\rm 3D}$ and Frontier Fields, over a consistent physical radial range.

Due to the differing redshifts of the samples, it is impossible to compare all samples across a common radial range without including radial regions that are either within the PSF or beyond the kinematic coverage of the data. The PSF region for MAGPI and Frontier Fields objects is comparable in size to the galaxy effective radii, whereas for ATLAS$^{\rm 3D}$ the PSF is less than 10 per cent of the median effective radius for that sample.

To make the comparison of total density slopes across studies fair, we re-compute total density slopes for the ATLAS$^{\rm 3D}$ and Frontier Fields samples using identical radial bounds as for MAGPI galaxies. Across samples and for all galaxies we define the radial bounds as $r = [R_{\rm e}/10, 2\,R_{\rm e}]$. The total density slope is then calculated as a 1D power-law fit to the analytic total profile within these radial bounds.

For Frontier Fields, there are 68/90 galaxies with kinematics at least beyond $2R_{\rm e}$; however, due to the PSF of ~ 0.6 arcsec FWHM across the fields the total slope calculation is extrapolated to radii smaller than the PSF.

For ATLAS$^{\rm 3D}$, there are only 18/258 galaxies with $v_{\rm rms}$ fields up to $2R_{\rm e}$ (Emsellem et al. 2011), and so for most objects we measure the total density slope by extrapolating beyond the region of kinematics used to constrain the total potential. That is, it is assumed that the total potential constrained by kinematics up to $1R_{\rm e}$ is the same potential that would be constrained if the object had kinematics extending to $2R_{\rm e}$. The end-to-end simulations presented in Appendix A imply this is the case, since there is no change on the input versus output inner density slope as the kinematic coverage is increased (see far right columns of Fig. A1).

Of the 30 galaxies in MAGPI judged as viable for measurement of the total slope, 20 have kinematics that extend to $2R_{\rm e}$, and 10 have kinematics that extend somewhere between 1.5 and $2R_{\rm e}$. For these 10 objects, the total slope measurement is extrapolated beyond the region of kinematics, and for all 30 objects the total slope measurement is extrapolated to within the PSF.

Finally, there is a break in the relation between velocity dispersion and the total density slope (Poci et al. 2017; Li et al. 2019). Galaxies with a central velocity dispersion below $\sim$100 km s^{-1} have a strong

Downloaded from https://academic.oup.com/mnras/article/522/3/3602/7152361 by Universiteit Leiden - LUMC user on 21 February 2024

trend with total density slope, but above $\sim$100 km s^{-1} there is only a mild correlation driven by morphological type. To remove the velocity dispersion as confounding factor, we further select galaxies across the samples that have a central velocity dispersion greater than 100 km s^{-1}. This cut mainly affects the ATLAS^{3D} sample. This final sample cut leaves 28 galaxies from MAGPI, 150 galaxies from ATLAS^{3D}, and 64 galaxies from the Frontier Fields clusters.

Total masses were calculated as twice the (spherical) mass integrated from the best-fitting potential within $1R_e$, as in Cappellari et al. (2013a). This calculation depends on the effective radius, density at the break radius, ρ_s, and inner density slope, γ'. Errors on the total masses were determined using the standard deviation of 100 masses calculated from random samples of the EMCEE chains. Errors on the total slope were calculated in the same way, by drawing 100 random samples of the estimated posterior distribution to construct the total density profile, and measuring the single power-law slope from that. All total masses and slopes are presented in Appendix C (Table C1).

We have re-calculated the total density slopes for Coma, SLUGGS, and Horizon-AGN to match the radial range used for the MAGPI, Frontier Fields, and ATLAS^{3D} sample, being $r = [\mathrm{R_e}/10, 2\,\mathrm{R_e}]$. While this does not alleviate issues of methodological biases, we believe it does aid comparison between studies. A summary of the radial ranges and slopes for all studies are given in Appendix C (Table C2).

4 RESULTS

Fig. 7 shows all the kinematic fields and Jeans models for the 30 MAGPI galaxies with $1R_e$ greater than the PSF FWHM and with kinematic coverage to at least $1.5R_e$. As mentioned above, two of these galaxies (1205197197 and 1205196165) have a velocity dispersion too low to be included in the final analysis of total density slopes (that is, they are not used to compute median value or correlations). We also include a foreground object at $z \sim 0.1$ and background object at $z \sim 0.5$, as both met the data quality requirements.

Table C1 includes the IDs, right ascensions and declinations, redshifts, central velocity dispersions, total mass, circularized effective radius, and total density slope with associated uncertainty for these 30 galaxies. Due to the data quality cuts imposed on the sample the formal uncertainties on the total density slope are small, and comparable to local Universe studies like that of Bellstedt et al. (2018). In the following sections, we assess the kinematic fits, compare the MAGPI total density slopes to the Frontier Fields and ATLAS^{3D} sample, compare to other dynamical and lensing works, compare to the predictions of simulations. We also investigate any correlations between the total density slope and other parameters.

The median density slope for the 28 MAGPI galaxies is $\gamma = -2.22 \pm 0.05$ (standard error on the median), with a sample standard deviation of 0.22. If all visually classified spiral galaxies are excluded (8 objects), the results are consistent within the uncertainties with a median of $\gamma = -2.23 \pm 0.04$ and a sample standard deviation of 0.15. In all of the following, the results do not depend on whether these spiral galaxies are excluded and so we leave them in the final sample.

4.1 Assessment of kinematic fits

Most of the MAGPI galaxies (24/30) have reduced χ^2 values less than three. MAGPI galaxies 1 207 197 197 and 1 204 198 199 have the highest reduced χ^2 values of $\sim$6, both with clear structure in their residuals maps in Fig. 7. MAGPI galaxy 1 207 197 197 in particular has a photometric twist that was not captured in our constant position angle MGE model. Similarly, 1 207 128 248 has particularly high residuals, although this object has a reduced χ^2 value of roughly one due to its high kinematic uncertainties, incorporated into the EMCEE determination of estimated parameters for the potential. Although spirals are generally well represented with a disc potential, they may also have bars that are not accounted for in the Jeans axisymmetric framework. MAGPI object 1 204 198 199 may have a bar which drives the higher discrepancy between the model and observed $v_{\rm rms}$ fields. In some cases, the spiral systems have $v_{\rm rms}$ models that match the observations particularly well, such as object 1204135171, at $z \sim 0.1$.

We split our sample into galaxies with χ^2 values below or equal to two ($N = 12$) and those with χ^2 values greater than two ($N = 16$), to test whether our conclusions are driven by the poorer kinematic fits. There is a non-significant difference between the two samples using a Kruskal–Wallis test statistic (p value $= 0.05$), and the derived medians are consistent within uncertainties ($\gamma = -2.30 \pm 0.14$ for reduced χ^2 values less or equal to 2, and $\gamma = -2.17 \pm 0.1$ for reduced χ^2 values greater than 2).

4.2 Comparison to Frontier fields and ATLAS^{3D}

Fig. 8 shows the distribution of MAGPI total density slopes as a function of redshift, with the slopes for the ATLAS^{3D} sample and Frontier Fields sample re-calculated with our new radial constraints.

The median density slope for MAGPI galaxies of $\gamma = -2.22 \pm 0.05$ compares well to that of the ATLAS^{3D} galaxies in the local Universe, with $\gamma = -2.25 \pm 0.02$. The re-analysed total density slopes of the Frontier Fields galaxies have a median of $\gamma = -2.01 \pm 0.04$, which is significantly shallower than for the MAGPI galaxies. This median value is different to the published value in Derkenne et al. (2021) of $\gamma = -2.11 \pm 0.03$ due to the additional data quality cuts made in this work, and the re-measurement of the slope between 0.1 and $2R_e$. The bottom panel of Fig. 8 shows the CDF of three samples, with the Frontier Fields sample shifted towards shallower values compared to the overlapping MAGPI and ATLAS^{3D} samples in this space.

Two statistical tests were carried out to assess the differences in the population of total density slopes calculated from MAGPI, ATLAS^{3D}, and the Frontier Fields sample. A Kruskal–Wallis test was used to test the null hypothesis of whether the populations share a median value, and an Anderson–Darling test was used to evaluate the null hypothesis that the observed samples originated from the same underlying distribution (considering the shape of the distribution as well). We found a significant difference between the MAGPI and Frontier Fields total density slope distributions, but no significant difference between the MAGPI and ATLAS^{3D} total density slope distributions.

The MAGPI galaxies studied are, on average, larger and more massive than the galaxies studied in the Frontier Fields work (see Fig. 9). Could these sample differences drive the observed differences in total density slopes? If the three comparison samples (MAGPI, ATLAS^{3D}, and Frontier Fields) are cut to a common size range of 3−8 kpc, there is still a significant difference between the MAGPI and Frontier Fields sample, and still no significant difference in the observed populations of total density slopes from MAGPI and ATLAS^{3D}. Similarly, if a common mass cut is made comparing only galaxies with a spherical total mass between $10^{10.5}$ and $10^{11.5}$ M$_\odot$ the results still hold. We note however that the samples become considerably smaller that makes the statistical comparison less sound. For all statistical tests, see Table 2.

Downloaded from https://academic.oup.com/mnras/article/522/3/3602/7152361 by Universiteit Leiden - LUMC user on 21 February 2024

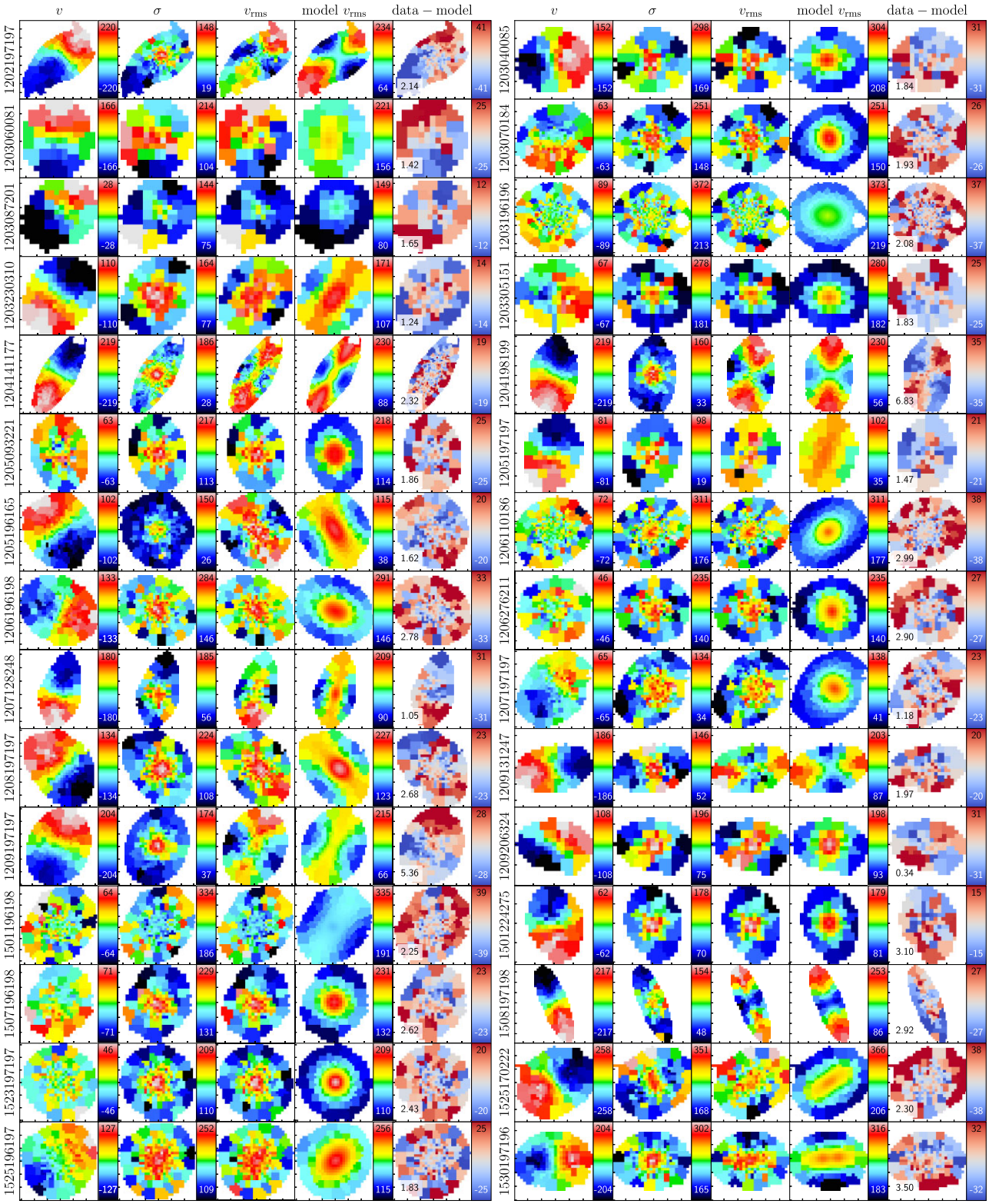

Figure 7. The velocity, velocity dispersion, observed $v_{\rm rms} = \sqrt{v^2 + \sigma^2}$ field, JAM modelled $v_{\rm rms}$ field, and residual field for each galaxy used in this work. The units for all panels are km s^{-1}. The modelled $v_{\rm rms}$ field shares the same colour scale as the observed $v_{\rm rms}$ field. The reduced χ^2 value is inset on the residual pane for each galaxy. The *x*- and *y*-axis ticks are 1 arcsec intervals. The MAGPI ID of each galaxy is given on the side of each row.

Downloaded from https://academic.oup.com/mnras/article/522/3/3602/7152361 by Universiteit Leiden - LUMC user on 21 February 2024

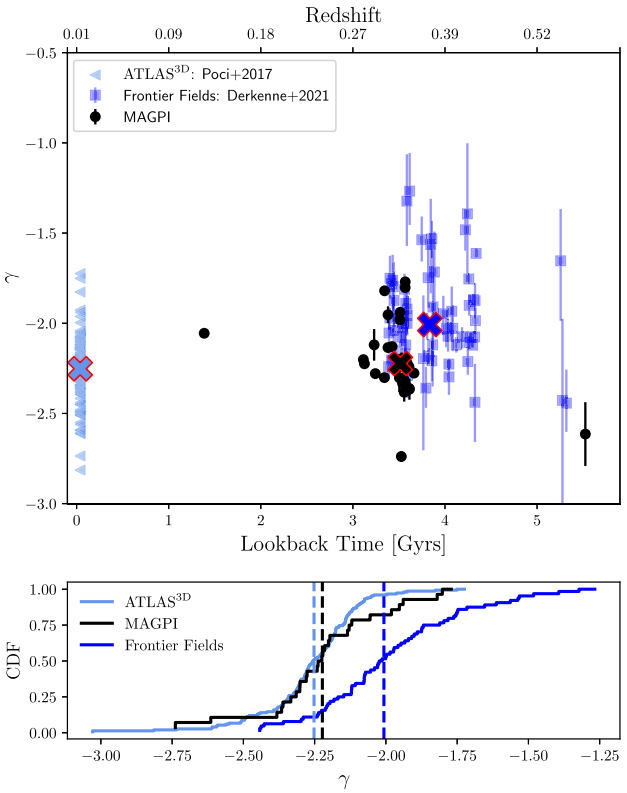

Figure 8. Top: The total density slope as a function of redshift/look-back time for the MAGPI sample and two main comparison samples: Frontier Fields and ATLAS^{3D}. The MAGPI values are shown in black, Frontier Fields as navy blue squares, and ATLAS^{3D} as light blue triangles. Filled crosses show the median values. Bottom: The cumulative distribution function (CDF) of the MAGPI, Frontier Fields, and ATLAS^{3D} samples. Vertical dashed lines indicate the sample medians.

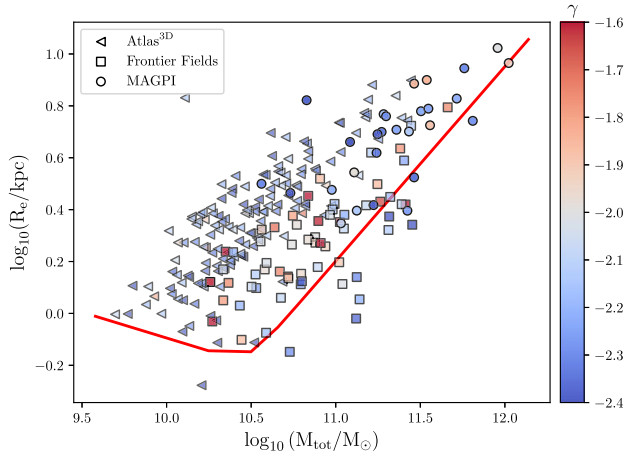

Figure 9. The *total* mass–size plane for the comparison samples with central velocity dispersion >100 km s^{-1}. The x-axis shows total dynamical masses, defined as twice the (spherical) mass integrated from the best-fitting potential within $1R_e$, as in Cappellari et al. (2013a). Since the total masses are in part constructed from the total density slopes, the Frontier Fields galaxies by construction have higher masses for their sizes due to their on average shallower total density slopes. The y-axis shows circularized effective radii, with radii for Frontier Fields galaxies from Derkenne et al. (2021), and radii for ATLAS^{3D} galaxies from Cappellari et al. (2011). The MAGPI circularized effective radii are shown in Table C1. The red solid line shows the 'Zone of Exclusion' in the ATLAS^{3D} survey mass–size plane from Cappellari et al. (2013b).

We conclude the ATLAS^{3D} and MAGPI total density slopes share a common distribution, but that the MAGPI and Frontier Fields slope distributions are significantly different. We stress that the MAGPI models and Frontier Fields Jeans models and parameter estimations were constructed in an almost identical manner, and argue that the difference in median total density slope of the two populations has a physical origin. As the Frontier Fields total density slopes represent galaxies in extreme, dense environments, we interpret this difference in slope distribution as being due to host environment. The consistency of the total slope distributions between the MAGPI and ATLAS^{3D} samples then indicates no evolution in the total slope across 3−4 Gyr of cosmic time.

The Frontier Fields galaxies are generally more compact than MAGPI galaxies, yet exhibit shallower total density slopes. That the Frontier Fields galaxies have shallower total density slopes for a more compact luminous component indicates they could have higher dark matter fractions than the MAGPI sample.

If the difference in total slope distributions between the MAGPI and Frontier Fields sample is due to host environment, we can also explore the impact on environment within the ATLAS^{3D} sample itself. The ATLAS^{3D} sample is drawn from a mixture of field galaxies and those from the local Virgo cluster, with 37/150 of the ATLAS^{3D} galaxies analysed in this work drawn from Virgo. Fig. 10 shows the distribution of ATLAS^{3D} total density slopes from the field and those from within the Virgo cluster. There is evidence of a mild offset between the total slopes of galaxies in Virgo and those from the field, although the Kruskal–Wallis and Anderson–Darling statistical tests are unable to discriminate between them. The Virgo slopes are slightly more shallow, which agrees with the observed difference between MAGPI and Frontier Fields slopes. We explore why we see a pronounced difference between MAGPI and Frontier Fields slopes but not between the field and Virgo ATLAS^{3D} samples in Section 5.

4.3 Comparison to other dynamical and lensing works

In this section, we compare to other literature studies with different methodologies and systematics. We show these literature results, as well as the predictions of the Horizon-AGN, IllustrisTNG, and Magneticum simulations, on Fig. 11. To fully understand how the methodological choices made in each study impact the resulting total density slopes it would be necessary to use complementary methods on the same sample, which is beyond the scope of this work.

The total slopes of galaxies in the Coma cluster (Thomas et al. 2011), shown on Fig. 11 in light green, are similarly shallow to the Frontier Fields galaxies. The median total density slopes for 17 galaxies in the Coma cluster is -2.00 ± 0.06, which is consistent with the Frontier Fields median of $\gamma = -2.01 \pm 0.04$. However, we note the generalized orbit-superposition technique of Schwarzschild modelling was used to constrain the total potential for that work, rather than axisymmetric Jeans modelling used for Frontier Fields galaxies. The consistency suggests the internal mass distribution of a galaxy is partly a function of its environment, with no evolution in the total slope across equivalent environments in the past 5 Gyr.

The median total density for MaNGA galaxies in the local Universe are shown on Fig. 11 as a red circle (Li et al. 2019). For that work, a mass-weighted inner density slope definition was used within $1R_e$, and a free scale radius (as opposed to the 20 kpc fixed scale radius used in this work). The MaNGA total density slope

Downloaded from https://academic.oup.com/mnras/article/522/3/3602/7152361 by Universiteit Leiden - LUMC user on 21 February 2024

Table 2. Column 1 lists the samples compared against each other in a two-way test. Mass cut means all samples are restricted to include galaxies within a cross-sample common mass range of $10^{10.5} - 10^{11.5}$ $M_\odot$. Radius-cut means all samples are restricted to only include galaxies within the common radial range 3−8 kpc – see Fig. 9 for the distributions of the three samples in the mass–size plane. KW = Kruskal–Wallis, AD = Anderson–Darling. The PYTHON implementation of the Anderson–Darling test (SCIPY.STATS) has p values clipped between 0.25 and 0.001. The median total slope is shown with the median standard error. In all tests, the MAGPI and ATLAS^{3D} sample medians are consistent, but the MAGPI and Frontier Fields sample medians are inconsistent.

Sample	KW p value	ADp value	MAGPI γ	Frontier fields γ	ATLAS^{3D} γ
MAGPI, Frontier Fields	9.5×10^{-5}	<0.001	-2.22 ± 0.05	$\gamma = -2.01 \pm 0.04$	–
MAGPI, ATLAS^{3D}	0.28	0.20	-2.22 ± 0.05	–	-2.25 ± 0.02
MAGPI, Frontier Fields (mass cut)	4×10^{-4}	<0.001	-2.24 ± 0.06	-2.03 ± 0.04	–
MAGPI, ATLAS^{3D} (mass cut)	0.94	>0.25	-2.24 ± 0.06	–	-2.26 ± 0.02
MAGPI, Frontier Fields (radius cut)	0.002	0.002	-2.23 ± 0.06	-1.87 ± 0.09	–
MAGPI, ATLAS^{3D} (radius cut)	0.77	>0.25	-2.23 ± 0.06	–	-2.26 ± 0.02

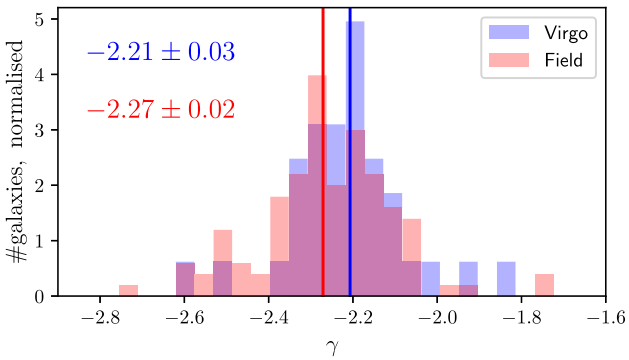

Figure 10. The distribution of total density slopes for ATLAS^{3D} galaxies within the Virgo cluster and from the field. There is evidence of the Virgo total slopes being mildly more shallow than for ATLAS^{3D} galaxies not in the Virgo cluster.

is equivalently steep to the MAGPI and ATLAS^{3D} samples, with median value $\gamma = -2.22 \pm 0.006$.

The SLUGGS data are shown as orange crosses on Fig. 11. The same break radius and total potential definition were used in that work in combination with Jeans modelling to constrain the total density slope. These galaxies are a subset of the ATLAS^{3D} sample, where ATLAS^{3D} stellar IFU data were coupled with globular cluster data at large radii. The median total density slope for this data is -2.06 ± 0.04, which is much shallower than the MAGPI or ATLAS^{3D} medians, and not consistent with our proposed scenario of environmental impact on the internal mass distribution. The shallower SLUGGS slopes could be due to the combination of globular cluster data with stellar IFU data, or could be due to the extended radial coverage of the SLUGGS data.

We also show published total density slopes from several gravitational lensing works, specifically those of Auger et al. (2010), Barnabè et al. (2011), Ruff et al. (2011), Bolton et al. (2012), Sonnenfeld et al. (2013), and Li et al. (2018), covering a combined redshift range of $0.06 < z < 1$. Li et al. (2018) note a significant dependence on the radial range used to calculate the slope, in that for a fixed galaxy the slope becomes steeper for an increasing radial range. Although likely due to different methodological reasons than those noted in this work, the bias works the same way as in this work. In general, the Einstein radius is used to constrain the gravitational potential in lensing studies, which is typically on a scale equivalent to the effective radius. We present MAGPI, Frontier Fields and ATLAS^{3D} slopes calculated on a similar radial range to the lensing works in Appendix B and Table C2. Regardless of the exact range used, the lensing slopes are more shallow than the MAGPI ones for similar redshifts.

Furthermore, lensing works with large redshift baselines show an evolution of the total slope from shallow at early times to steeper in the local Universe (Ruff et al. 2011; Bolton et al. 2012; Li et al. 2018). This is tension with our finding that, across a smaller redshift baseline, that there has been no evolution in the total density slope between MAGPI and ATLAS^{3D} galaxies. Even if there is a methodological offset when comparing the techniques, this discrepancy regarding the evolution remains. Galaxies that act as gravitational lenses are necessarily massive and dense, but the evolution with redshift is found to hold even after considering other parameters such as stellar mass and radius, and radial range used to constrain the slope (Bolton et al. 2012; Li et al. 2018). We note the distribution of total density slopes has large intrinsic scatter, and so increasing sample sizes at higher redshifts, with complementary methods, will be crucial to determining the slope evolution.

4.4 Comparison to simulations

In Fig. 11, we show a comparison to three simulations: Magneticum, IllustrisTNG, and Horizon-AGN. The IllustrisTNG total density slopes, and the Horizon-AGN total density slopes in the redshift range $0.018 < z < 0.305$ are consistent within the uncertainties, and show little to no evolution in this span of cosmic time. The Horizon-AGN slopes do become marginally steeper for $z < 0.3$, from $\gamma \sim -1.93$ to $\gamma \sim -1.99$, but this is still consistent with no evolution in this period. This agrees with the lack of evolution seen between the MAGPI and ATLAS^{3D} slopes, and broadly consistent with the Magneticum results, as a wider redshift baseline is needed before the predictions become significantly different.

Around the nominal MAGPI redshift of 0.3, the simulation slopes are on average more shallow than the MAGPI ones. In the local universe the median total density slopes from all simulations considered here are more shallow than the ATLAS^{3D} median, comparing $\gamma = -2.25 \pm 0.02$ to roughly $\gamma = -2.0$, but are similar to the Frontier Fields median. In Fig. 12, we show the size–mass plane for Magneticum, Horizon-AGN, Frontier Fields, and MAGPI galaxies at $z \sim 0.3$. At fixed stellar mass, the simulated galaxies are typically more extended in radius than either the MAGPI or Frontier Fields samples. A small set of Magneticum galaxies approximate the size–mass distribution of MAGPI galaxies, and have more similar total density slopes. In general, however, the simulated and observed samples do not overlap. There is also a visible correlation particularly along the radius-axis between simulated galaxies and total density slope, in that galaxies with larger radii tend to have shallower

Downloaded from https://academic.oup.com/mnras/article/522/3/3602/7152361 by Universiteit Leiden - LUMC user on 21 February 2024

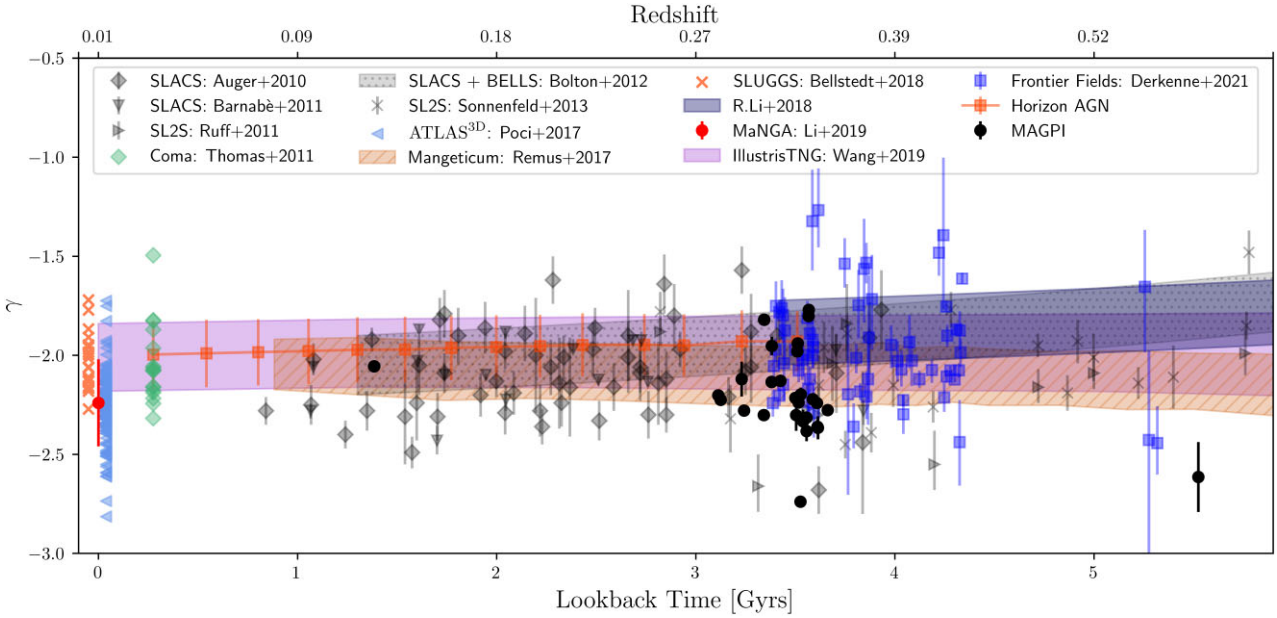

Figure 11. Top: The total density slope as a function of redshift/look-back time. The MAGPI values are shown in black, Frontier Fields as navy blue squares, and ATLAS^{3D} as light blue triangles. Data points for Coma are shown as green diamonds using models from Thomas et al. (2011). At redshift zero are also shown total density slopes from Bellstedt et al. (2018) (orange crosses) and from the MaNGA survey as an average (red circle) with standard deviation (Li et al. 2019). These points have been slightly offset in the x direction for visibility. Dark grey symbols show total density slopes measured using gravitational lensing techniques (Auger et al. 2010; Barnabè et al. 2011; Ruff et al. 2011; Sonnenfeld et al. 2013). The grey dotted band shows the fitted relation, of width 1σ, between total density slopes and redshift from Bolton et al. (2012), of the form $\gamma(z) = (-2.11 \pm 0.02) + z(0.6 \pm 0.15)$. The blue band shows a relation from Li et al. (2018) of the form $\mathrm{d}\langle\gamma\rangle/\mathrm{d}z = 0.309^{+0.160}_{-0.166}$. The orange striped band shows the average total density slopes from the Magneticum simulations with a 1σ width (Remus et al. 2017). The purple band shows the average total density slopes from the IllustrisTNG with a 1σ width (Wang et al. 2019). The dark orange squares show the Horizon–AGN total density slopes, computed as a single power-law slope in the radial range of $0.1-2R_e$, and 1σ width.

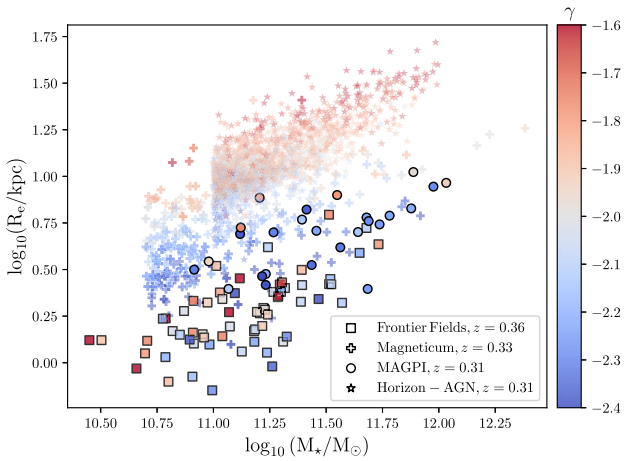

Figure 12. The size–mass plane for Magneticum, Horizon-AGN, MAGPI, and Frontier Fields galaxies at $z \sim 0.3$; for the MAGPI and Frontier Fields samples this is the mean redshift, and for Magneticum and Horizon-AGN this corresponds to a single snapshot. For Magneticum, the 3D half-mass radius, $R^{3D}_{1/2}$, is plotted. The simulated galaxies are more extended for equivalent stellar masses than MAGPI galaxies.

total density slopes at fixed mass. We explore these correlations in Section 4.5.

We therefore stress that the simulated and observed galaxies do not overlap well in the mass–size plane, and this difference could be intertwined with the offset in total density slope medians between the different samples, seen in Fig. 11.

We used the Magneticum and Horizon-AGN galaxies to test whether the separation of total slopes with environments also exists in the simulations, shown in Fig. 13. To do this, galaxies were binned by virial mass of the main host galaxy. We used these divisions as a proxy for environment, where the bins represent: small galaxies, in a halo mass bin between 1×10^{12} M$_\odot$ and 3×10^{12} M$_\odot$; massive galaxies in a halo between 3×10^{12} M$_\odot$ and 1×10^{13} M$_\odot$; galaxies in groups with halo mass between 1×10^{13} M$_\odot$ and 1×10^{14} M$_\odot$; and galaxies in cluster environments, with a host halo mass greater than 10^{14} M$_\odot$.

The 'cluster' bin is still less massive than the Frontier Fields clusters of order 10^{15} M$_\odot$. None the less, a trend is clearly visible in the Magneticum simulation, where galaxies belonging to more massive haloes have shallower total density slopes than those in less massive haloes. Partly this is due to the trends in the Magneticum simulation between stellar mass and total density slope (see Section 4.5), and stellar mass and halo mass are themselves correlated. However, a linear model for Magneticum total slopes has more predictive power and a lower Akaike information criterion (AIC) when both stellar mass and halo mass are used as explanatory variables rather than stellar mass alone (−350 compared to −224). Therefore, we conclude there exists a dependence between total density slope and host halo mass. This dependence in the Magneticum simulations supports our finding of environmental difference in internal mass distribution between MAGPI and Frontier Fields galaxies. From Fig. 13, we also see that the Magneticum total density slopes reach MAGPI-like values at $z \sim 0.8$, which could be related to the size–mass offset in samples discussed above.

For the Horizon-AGN galaxies, there is again a separation in total density slopes between the small galaxy, massive galaxy, and

Downloaded from https://academic.oup.com/mnras/article/522/3/3602/7152361 by Universiteit Leiden - LUMC user on 21 February 2024

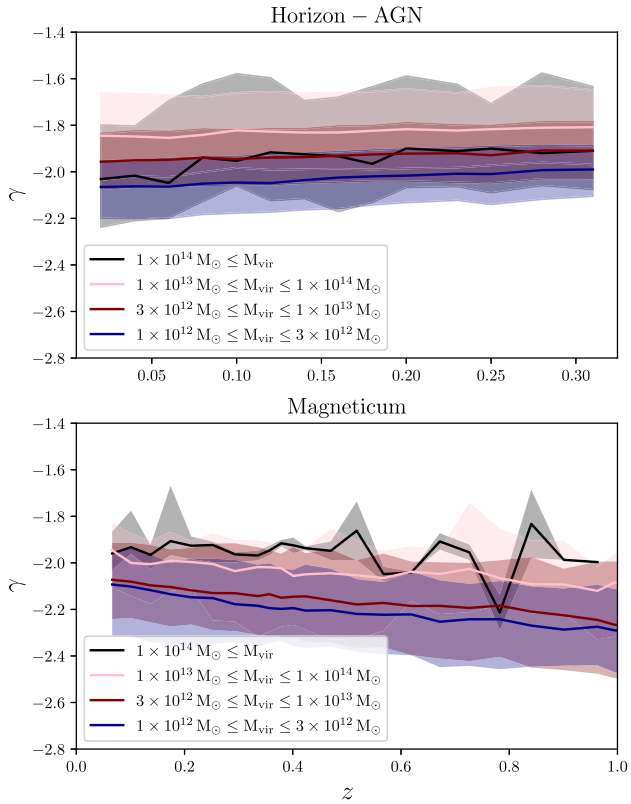

Figure 13. Top: Horizon-AGN galaxies divided into host halo mass bins. The blue line shows small galaxies with virial mass of the main host halo between 1 and 3×10^{12} $M_\odot$, the maroon line shows massive galaxies with host halo mass between 3×10^{12} $M_\odot$ and 1×10^{13} $M_\odot$, the pink line shows galaxies in groups with host halo mass between 1×10^{13} $M_\odot$ and 1×10^{13} $M_\odot$ and 1×10^{14} $M_\odot$, and finally the black line shows galaxies in cluster environments, with a host halo mass greater than 10^{14} $M_\odot$. The shading represents the standard deviation. Bottom row: Magneticum galaxies from Remus et al. (2017) with the same cuts as the Horizon-AGN galaxies. The cluster masses in Magneticum are not as massive as the Frontier Fields environments, but a division between total slope and host mass is still seen. As with the different in total density slope between MAGPI and Frontier Fields galaxies, Magneticum galaxies in denser environments (clusters) have on average shallower total density slopes. For Horizon-AGN galaxies, the trend is the same for groups, massive galaxies, and small galaxies, except clusters no longer have the most shallow slopes.

group bins, which follows the trend observed with Magneticum galaxies. However, the cluster bin has slopes comparable to small or massive galaxies, and it is the group galaxies that have the most shallow slopes on average. As with Magneticum galaxies, a linear model including both stellar mass and dark matter halo mass has more predictive power than stellar mass alone using the AIC (−2444 compared to −2433). The disagreement regarding the environmental trend for the cluster could stem from differences in the sample selection criteria. For instance, in Horizon-AGN, both the brightest cluster galaxy and relatively small satellites within the cluster region are excluded from the sample stellar mass range of 10^{11}–10^{12} $M_\odot$.

4.5 Correlations with the total density slope

We investigate whether there exist any significant correlations between the total density slope and other intrinsic galaxy parameters, such as central velocity dispersion, effective radius, total mass, stellar mass, and stellar mass surface density. For the ATLAS^{3D} galaxies, we take circularized effective radii from Cappellari et al. (2011) and the central velocity dispersion from Cappellari et al. (2013a). For Frontier Fields galaxies the circularized effective radii and central velocity dispersions are from Derkenne et al. (2021). Total masses were calculated in the same way for all three samples, defined as twice the mass integrated given the median parametrization of the potential within a sphere of one effective radius (Cappellari et al. 2013a).

Stellar masses for MAGPI were calculated using the spectral energy distribution fitting software PROSPECT with a Chabrier (Chabrier 2003) initial mass function. The spectral energy distribution was fit using pixel-matched imaging in the *ugriZYJHKs* bands from the GAMA survey (Bellstedt et al. 2020), with photometry derived by the MUSE-based PROFOUND segmentation maps for each galaxy. For the ATLAS^{3D} sample, stellar masses were calculated as the total luminosity from the MGEs of Scott et al. (2013) multiplied by the SDSS *r*-band mass-to-light ratio from Cappellari et al. (2013b), giving a total stellar mass. For the Frontier Fields sample, *V*-band stellar mass-to-light ratios were calculated from an MILES (Vazdekis et al. 2010) template library PPXF spectral fit with a saltpeter (Salpeter 1955) initial mass function. These were converted to a Chabrier initial mass function by dividing by 1.53, as in Driver et al. (2011). The total stellar mass was then calculated as the total luminosity from the MGEs multiplied by this mass-to-light ratio.

The stellar surface mass density is given as

$$\Sigma_\star = \frac{M_\star}{2\pi R_e^2}. \tag{6}$$

The relations are plotted in Fig. 14, and all significant relations are given in Table 3. The MAGPI galaxies show no significant correlation with any other parameter, possibly due to the small sample size. For the velocity dispersion, this could also be due to the greater mix of morphological type, as early-type galaxies have a slight negative trend between slope and velocity dispersion, whereas spiral galaxies do not (Li et al. 2019). The only other parameter the observational sample correlates with is the stellar mass surface density, which is intuitive as galaxies that are more compact have steeper slopes.

We also compared to the trends seen in simulations, using the sample of Horizon-AGN and Magneticum galaxies, as well as the linear correlations published in Wang et al. (2020). Interestingly, the simulations all predict that galaxies with greater velocity dispersions have shallower total density slopes, although for the observational sample we see the opposite. This discrepancy continues with the stellar mass, as simulations predict the more massive the stellar content of a galaxy the more shallow its total slope, whereas the observational samples show no trend to a mildly negative one. For the ATLAS^{3D} and MAGPI samples, the trends between total slope and stellar mass surface density (although not significant for MAGPI) are quite close to the ones seen for Magneticum, Horizon-AGN, and IllustrisTNG galaxies. The Frontier Fields galaxies show the same trend (the more compact a galaxy is the steeper its total slope); however, the galaxies are offset from the simulated relations. The correlation between stellar surface density and total density slopes is also seen in the measurements from gravitational lensing (Sonnenfeld et al. 2013).

A potential reason for the difference in observed trends between the simulation and observational works is the manner in which the

Downloaded from https://academic.oup.com/mnras/article/522/3/3602/7152361 by Universiteit Leiden - LUMC user on 21 February 2024

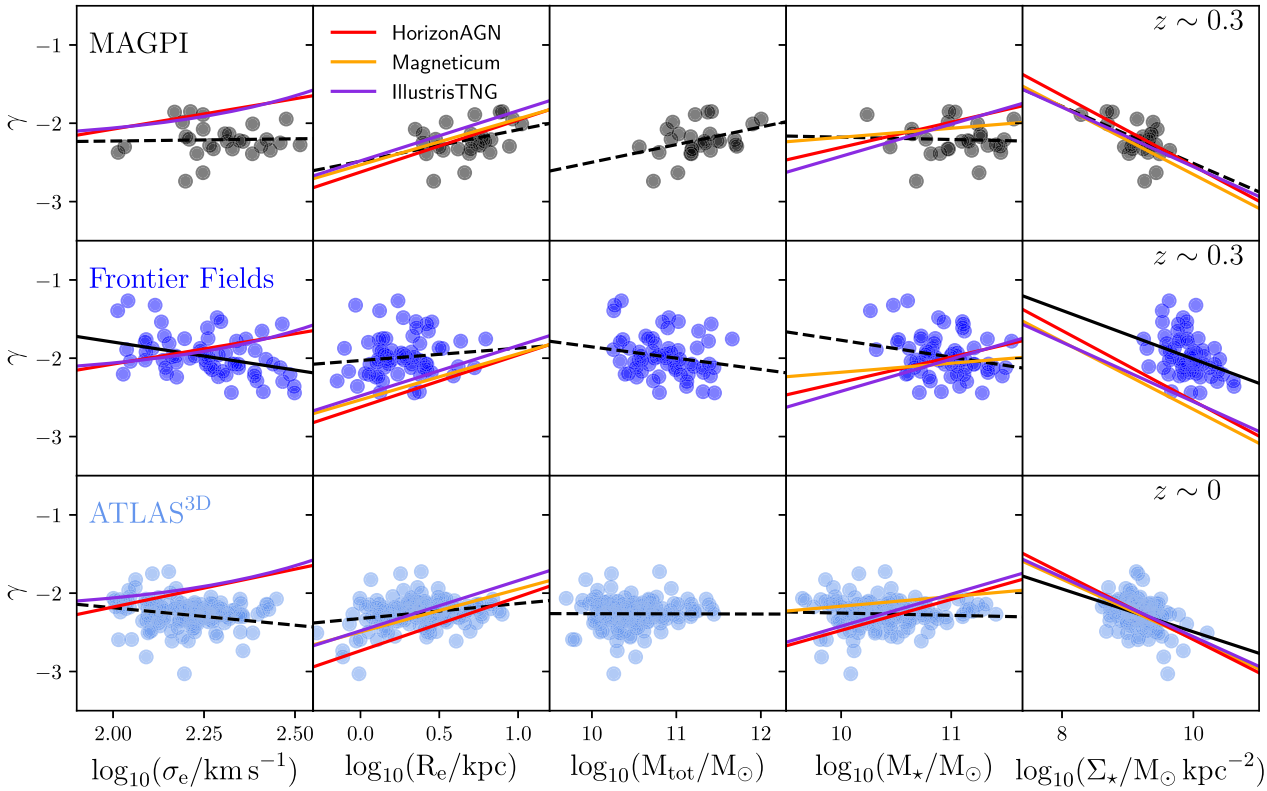

Figure 14. Linear correlations between the total density slope and other galaxy parameters: central velocity dispersion, effective radius, total mass, stellar mass, and stellar mass surface density. For the MAGPI, Frontier Fields and ATLAS^{3D} samples, panels with a black dashed line indicates a non-significant fit with a p value greater than 0.01. Solid black lines show correlations with a p value smaller than 0.01, fitted using the PYTHON package LTSFIT (Cappellari et al. 2013a) and of the form $y = a + b(x - x_0)$, where x_0 is the median of the x-values. The IllustrisTNG correlations are taken directly from Wang et al. (2020) at $z = 0$, and the central velocity dispersion is $\sigma_{e/2}$ instead of σ_e. Horizon-AGN correlations are shown for galaxies from the simulation snapshot at 0.305 on the MAGPI and Frontier Fields rows, and for galaxies from the redshift 0.018 snapshot for the ATLAS^{3D} row. Likewise, Magneticum correlations are shown for galaxies including snapshots between $0.25 < z < 0.35$ on the MAGPI and Frontier Fields rows, and for galaxies in snapshots with $z < 0.1$ for the ATLAS^{3D} row. All significant relations are given in Table 3.

Table 3. A summary of the linear correlations between the total slope and parameters shown in Fig. 14. Only significant correlations with a Spearman p value of less than 0.01 are shown. Correlations with total mass are not given in this table, as no trends were significant for the MAGPI, ATLAS^{3D}, and Frontier Fields samples. We fit each data set using the PYTHON package LTSFIT (Cappellari et al. 2013a), and given relations for the total slope are of the form $y = a + b(x - x_0)$, where x_0 is median of the x values. For the IllustrisTNG relations, we take the correlations directly from Wang et al. (2020), with the gradient shown as m. The stellar surface mass density $\Sigma_\star$ is defined as $M_\star/2\pi R_e$. For IllustrisTNG, the correlation with velocity dispersion uses a central aperture dispersion $\sigma_{e/2}$.

Sample	$\log_{10}(\sigma_e/\mathrm{km\,s^{-1}})$	$\log_{10}(R_e/\mathrm{kpc})$	$\log_{10}(M_\star/M_\odot)$	$\log_{10}(\Sigma_\star/M_\odot\,\mathrm{kpc}^{-2})$
MAGPI	–	–	–	–
Frontier Fields	$-1.98 - 0.71(x - 2.27)$	–	–	$-1.99 - 0.31(x - 9.62)$
ATLAS^{3D}	–	–	–	$-2.26 - 0.27(x - 9.16)$
Magneticum, $z < 0.1$	–	$-2.04 + 0.55(x - 0.83)$	$-2.04 + 0.12(x - 11.02)$	$-2.05 - 0.38(x - 8.59)$
Magneticum, $0.25 < z < 0.35$	–	$-2.06 + 0.59(x - 0.79)$	$-2.06 + 0.12(x - 11.02)$	$-2.07 - 0.43(x - 8.65)$
Horizon-AGN, $z = 0.018$	$-2.00 + 0.97(x - 2.18)$	$-2.00 + 0.69(x - 1.07)$	$-2.01 + 0.40(x - 11.19)$	$-1.99 - 0.42(x - 8.58)$
Horizon-AGN, $z = 0.305$	$-1.93 + 0.78(x - 2.18)$	$-1.93 + 0.67(x - 1.04)$	$-1.93 + 0.32(x - 11.17)$	$-1.92 - 0.45(x - 8.62)$
IllustrisTNG, $z = 0$	$m = -0.00019$	$m = 0.64$	$m = 0.41$	$m = -0.45$

slopes are measured. As the simulations have access to the dark matter, star, and gas particles directly, the total density slope is measured by fitting a power law to the co-added simulation particles in spherical, concentric shells. What systematic differences this introduces when comparing the slopes to observational studies can be addressed in future work by constructing mock IFU observations of simulation data and re-measuring the slopes.

5 DISCUSSION

In our results, we have shown there is a significant difference in the distribution of total density slopes of MAGPI and Frontier Fields galaxies, with Frontier Fields galaxies having on average total density profiles with shallower slopes. This difference suggests the mass distribution of Frontier Fields galaxies are, on average, less centrally concentrated (the mass density falls off less rapidly with radius)

Downloaded from https://academic.oup.com/mnras/article/522/3/3602/7152361 by Universiteit Leiden - LUMC user on 21 February 2024

than for MAGPI galaxies. The differences observed in the total mass density slopes of the populations hold if the samples are cut to overlapping radii and mass ranges, and when cut by velocity dispersion to remove any potential trends with that parameter. The detailed methodology of deriving the total density slopes for MAGPI and Frontier Fields objects are near identical, and any dependence of total density slope with radial range is removed by measuring all slopes on the same radial range.

5.1 The Frontier Fields, Virgo, and Coma environments

A remaining difference between the samples is environment. The Frontier Fields galaxies are drawn from dense cluster environments, whereas MAGPI targets are drawn from a range of environments that includes field galaxies and galaxies in groups (see Foster et al. 2021 for a summary, in particular their fig. 4. Note we do not include any Frontier Field objects as part of the MAGPI sample in this work, although Frontier Fields clusters Abell 2744 and Abell 370 are supplementary to the MAGPI survey). The Frontier Fields clusters were selected as ideal candidates for lensing systems (Lotz et al. 2017), and all are massive and X-ray luminous. The clusters span $\sim 1 \times 10^{45}$ erg s^{-1} as a bolometric X-ray luminosity for MACSJ0416.1-2403 (Mann & Ebeling 2012), to $\sim 3 \times 10^{45}$ erg s^{-1} at 2–10 keV for Abell 2744 (Allen 1998).

The Frontier Fields clusters all show significant substructure, interpreted as evidence of ongoing formation and mergers (Zitrin & Broadhurst 2009; Richard et al. 2010; Mann & Ebeling 2012; Gruen et al. 2013), with Abell 2744 in particular having up to eight different mass concentrations (Jauzac et al. 2016). In fact, the structure of Abell 2744 is so extreme it has been used to question whether such a cluster is even possible within the Lambda cold dark matter (ΛCDM) model, as no equivalent clusters could be found within the Millenium XXL simulation volume (Schwinn et al. 2017), although such a structure has been identified in the Magneticum simulation suite with the detailed comparison of cluster and simulation masses depending on projection (Kimmig et al. 2022). Due to the complexity of the clusters, gravitational lensing has been effective in estimating total masses. Merten et al. (2011) place the total mass of Abell 2744 at M($r < 1.3$ Mpc) $= (1.8 \pm 0.4) \times 10^{15}$ M$_\odot$ with $h = 0.7$ using a mass model created from weak lensing, with mass estimates of the other clusters consistently falling above $M \sim 10^{15}$ M$_\odot$ (Williamson et al. 2011; Zheng et al. 2012; Grillo et al. 2015; Lagattuta et al. 2022).

There is little observed difference in total density slope between ATLAS^{3D} galaxies drawn from Virgo and those from the field. Virgo is less X-ray luminous than the Frontier Fields clusters, classified as having low X-ray luminosity ($< 10^{44}$ erg s^{-1}) and low central galaxy density (Jones & Forman 1984). Mass estimates also fall well below those of the Frontier clusters, with Simionescu et al. (2017) placing the virial mass of Virgo at $M_{200} = (1.05 \pm 0.02) \times 10^{14}$ M$_\odot$ for $r_{200} = (974.1 \pm 5.7)$ kpc. To stress the difference, a recent strong lensing analysis of Abell 2744 puts the total mass at $M = (1.77 \pm 0.07) \times 10^{14}$ M$_\odot$ at a radius of just 200 kpc (Bergamini et al. 2023).

In contrast to Virgo, Coma is more equivalent in its mass to the Frontier Fields clusters. A recent Bayesian deep-learning analysis of the mass of Coma by Ho et al. (2022) gives a mass of M$_{200} = 10^{15.10\pm0.15}\, h^{-1}$ M$_\odot$ within $(1.78 \pm 0.03)\, h^{-1}$ Mpc of the cluster centre (see their fig. 3 for this result compared to historical mass estimates). The X-ray luminosity of the cluster is also more than an order of magnitude greater than that of Virgo, at $\sim 8 \times 10^{44}$ erg s^{-1} in the band 0.1–2.4 keV (Reiprich & Böhringer 2002).

The nature of the Frontier Fields programme means studied galaxies are situated well within the core regions of the clusters because of the limited field of view of MUSE (Lotz et al. 2017). Due to the different observing strategy of the ATLAS^{3D} survey, the galaxies drawn from Virgo are not limited to the very core regions. This detail of survey design could also impact how comparable the two environments are, as the local density changes with distance from the cluster core. Li et al. (2019) found that satellites within haloes have a density slope that is steeper (more negative) than centrals by about $\sim$0.1. Although none of the galaxies modelled in Derkenne et al. (2021) are the 'brightest cluster galaxies' in the eight substructures identified by Jauzac et al. (2016), we might be comparing the very dense regions of the Frontier Fields clusters to a variety of local densities in Virgo. In future work, we aim to address this question quantitatively with MAGPI data, as the full sample will probe a large range of local environments, and we will be able to apply consistent metrics.

5.2 Drivers of the total slope

From the Magneticum simulations, it is known that progressive dry mergers drive total density slopes towards isothermal values (Remus et al. 2013). Once a galaxy has an isothermal total density profile, subsequent dry mergers do not perturb the slope away again. Dry mergers tend to increase the stellar mass at large radii, resulting in shallower total density slopes. Minor mergers in particular have increased efficiency with regard to size-growth compared to major mergers (Naab et al. 2009). Major merger rates for galaxies below $z = 0.5$ are uncommon, placed at an occurrence of just 0.058 ± 0.009 per Gyr (López-Sanjuan et al. 2015). Minor mergers are found to be $\sim$3 times more likely that major mergers at redshift $z = 0.7$ with little evidence the merger rate evolves with redshift below $z = 1$, making minor mergers also infrequent across the redshift baseline we consider (Lotz et al. 2011). That we see no evidence for evolution in the total density slope is therefore consistent with the low occurrence of mergers at later times. The evolution observed by gravitational lensing is potentially a factor of those works targeting massive galaxies, which are more likely to have undergone mergers and therefore have closer to isothermal slopes.

While galaxies in cluster environments move with high velocities and are unlikely to undergo mergers, galaxy clusters themselves are assembled from the in-fall of groups, as seen with the many substructures that make up the Frontier Fields clusters, and especially Abell 2744 (Jauzac et al. 2016). Galaxies in groups would experience higher merger rates at earlier times as local density and merger rates are coupled (Jian et al. 2012; Shankar et al. 2013; Watson et al. 2019). This is seen in the cold dark matter haloes as well, where haloes in high-density environments undergo most of their mass aggregation at earlier times compared to haloes is less dense environments (Maulbetsch et al. 2007). Papovich et al. (2012) studied a sample of galaxies in a proto-cluster at redshift $z = 1.62$, and found quiescent galaxies in clusters are larger than those in the field at that redshift. This implies, like the dark matter haloes, accelerated growth at higher redshifts for galaxies in cluster environments. Galaxies in clusters might therefore have undergone more mergers in their history than isolated fields galaxies, explaining why we see a difference in the internal mass distributions of galaxies in the MAGPI survey compared to those drawn from the Frontier Fields environments.

Ram-pressure stripping and harassment can also occur in the cluster environments, which in extreme cases can result in the unusual 'jellyfish' galaxies with extended gas streams and clumpy

Downloaded from https://academic.oup.com/mnras/article/522/3/3602/7152361 by Universiteit Leiden - LUMC user on 21 February 2024

star formation marking their violent fall into the cluster environment (Owers et al. 2012; Poggianti et al. 2017). As stars are preferentially stripped from a galaxy potential only after the majority of the dark matter (Smith et al. 2016), this suggests galaxies in a cluster potential with visible distortions of their stellar matter are also significantly transformed in their total mass distribution. This result is evidence of the cluster environment itself transforming the properties of a galaxy.

6 SUMMARY AND CONCLUSIONS

The MAGPI survey is a MUSE Large Programme survey observing massive galaxies in the 'middle-ages' of the Universe. With over 200 h of observing time on the VLT, this survey will enable the spatial mapping of ionized gas and stars in galaxies 3–4 Gyr ago, providing a detailed understanding of galaxy evolution spanning field to cluster environments. Foreground and background objects in the fields supplement this time baseline further.

In this work, we present an early study of the impact of environment in shaping the internal mass distributions of galaxies, with the intention of providing a quantitative relationship between environmental metrics and internal mass distribution when the full sample is observed. We present total mass density slopes for 28 galaxies in the MAGPI survey. To construct the density slopes, 2D resolved stellar kinematic maps measured from MUSE data are used in combination with multi-Gaussian models of the stellar light to construct Jeans dynamical models, with the total potential (baryons and dark matter) described by a generalized NFW profile.

We compare the MAGPI total density slope distribution primarily to two other works. First, the total density slopes for ATLAS^{3D} galaxies as measured using a consistent methodology by Poci et al. (2017). These galaxies are in the local Universe (<40 Mpc) and are from field environments and the Virgo cluster, a dynamically young cluster of moderate mass. Secondly, we compare to the density slopes from Frontier Fields galaxies as measured by Derkenne et al. (2021). These galaxies are all from extreme and dense cluster environments in the redshift range $0.29 < z < 0.55$. Combining these methodologically consistent studies allows us to trace the internal mass distribution of galaxies from field to cluster environments across 5 Gyr of cosmic time in a self-consistent manner.

We determined that the radial range across which the total slope is measured is critical when using a generalized NFW total potential with fixed break radius. A mismatch between radial ranges can cause the measured slope to change by $\sim$0.1, which erases the signature in density slope from host environment or other parameters. For this reason, we re-analyse total mass density slopes from ATLAS^{3D} and Frontier Fields galaxies using the same radial range as MAGPI galaxies. We measure total mass density slopes in the radial range $r = [R_e/10, 2R_e]$.

The main results are the following:

(i) We found a median total mass density slope of $\gamma = -2.22 \pm 0.05$ (standard error) for the MAGPI 28 galaxies with central velocity dispersion greater than 100 km s^{-1}. These results are unchanged if we consider only early-type morphology galaxies, with median slope $\gamma = -2.23 \pm 0.04$.

(ii) We found a median slope of $\gamma = -2.01 \pm 0.04$ for 68 Frontier Fields galaxies at median redshift 0.348, and a median slope of $\gamma = -2.25 \pm 0.02$ for 150 galaxies from the ATLAS^{3D} sample in the local Universe.

(iii) We found no difference between the distribution and median slope of MAGPI and ATLAS^{3D} galaxies, even after cutting the samples to common size and mass ranges. The similarity of the samples indicates the total density slope for galaxies in intermediate density environments has not evolved across the past 3−4 Gyr of cosmic time. The MAGPI and ATLAS^{3D} samples are treated as roughly equivalent in terms of their host environments in comparison to the very dense Frontier Fields cluster environments. This lack of evolution is broadly consistent with the hydrodynamical cosmological simulation results of Magneticum, IllustrisTNG, and Horizon-AGN. We do not see evidence of the density slope evolutionary trends derived from gravitational lensing studies.

(iv) A statistically significant difference is found in the distribution of total density slopes between the MAGPI and Frontier Fields sample ($\gamma = -2.22 \pm 0.05$ compared to $\gamma = -2.01 \pm 0.04$, respectively). This difference remains statistically significant when cutting the samples to common radius and mass ranges.

(v) The difference in slope distribution suggest that environmental factors play a role in the internal mass distributions of galaxies. Dense, cluster environments are more likely to host galaxies with shallow mass distributions than field environments, potentially due to the way clusters assemble their mass from galaxy groups. The separation of total density slopes with environment (as indicated by host halo mass) is also predicted by the Magneticum simulations. The dependence of slopes with environment in the Horizon-AGN simulations is not as clear.

For this work, we have used different galaxy samples to broadly categorize galaxies as residing in field, group, or cluster environments. When all MAGPI fields are observed we can expect to more than triple the sample size used here, which will allow for a quantitative test between environmental metrics (such as group number) and total density slope. The establishment of the impact of environment with total density slope in the 'Middle Ages' can be compared against local Universe surveys that span a wide range of environments, such as the SAMI survey or the recently commissioned Hector[3] survey. The launch of the *JWST* also makes it possible to push this type of resolved stellar kinematic methodology further back in cosmic time, where the predictions of the different simulations (and the measurements of gravitational lensing) significantly differ.

ACKNOWLEDGEMENTS

We thank the anonymous reviewer for their constructive feedback. We wish to thank the European Southern Observatory (ESO) staff, and in particular the staff at Paranal Observatory, for carrying out the MAGPI observations. MAGPI targets were selected from the Galaxy and Mass Assembly (GAMA) survey. GAMA is a joint European-Australasian project based around a spectroscopic campaign using the Anglo-Australian Telescope. GAMA is funded by the Science and Technology Facilities Council (UK), the Australian Research Council (ARC), the Australian Astronomical Optics, and the participating institutions. GAMA photometry is based on observations made with ESO Telescopes at the La Silla Paranal Observatory under programme ID 179.A-2004, ID 177.A-3016. CL, JTM, and CF are the recipients of an ARC Discovery Project DP210101945. CF is the recipient of an ARC Future Fellowship (project number FT210100168) funded by the Australian Government. CL, JTM, and EW acknowledge support by the Australian Research Council Centre of Excellence for All Sky Astrophysics in 3 Dimensions (ASTRO 3D), through project number CE170100013. FDE acknowledges funding through the European Research Council (ERC)

[3]https://hector.survey.org.au/

Downloaded from https://academic.oup.com/mnras/article/522/3/3602/7152361 by Universiteit Leiden - LUMC user on 21 February 2024

Advanced grant 695671 'QUENCH' and support by the STFC. AFM has received support from the Spanish Ministry grants CEX2019-000920-S, PID2021-123313NA-I00, and 4RYC2021-031099-I. PS is supported by the Australian Government Research Training Programme (RTP) Scholarship. PS also acknowledges support in the form of Oort Fellowship at Leiden Observatory, and the International Astronomical Union-Gruber Foundation Fellowship. LMV acknowledges support by the COMPLEX project from the ERC under the European Union's Horizon 2020 research and innovation programme grant agreement ERC-2019-AdG 882679. SKY acknowledges support from the Korean National Research Foundation (2020R1A2C3003769, 2022R1A6A1A03053472). GS thanks the South African Radio Astronomy Observatory postdoctoral fellowship grant (UID 97882). YP acknowledges National Science Foundation of China (NSFC) grants 12125301, 12192220, 12192222, and the science research grants from the China Manned Space Project with no. CMS-CSST-2021-A07. This research was conducted on the land of the Wallumattagal clan of the Dharug Nation.

DATA AVAILABILITY

The MAGPI spectral data underlying this work are available from the ESO Science Archive Facility (http://archive.eso.org/cms.html).

REFERENCES

Allen S. W., 1998, MNRAS, 296, 392
Auger M. W., Treu T., Bolton A. S., Gavazzi R., Koopmans L. V. E., Marshall P. J., Moustakas L. A., Burles S., 2010, ApJ, 724, 511
Barnabè M., Czoske O., Koopmans L. V. E., Treu T., Bolton A. S., 2011, MNRAS, 415, 2215
Bellstedt S. et al., 2018, MNRAS, 476, 4543
Bellstedt S. et al., 2020, MNRAS, 496, 3235
Bergamini P. et al., 2023, A&A, 670, A60
Bialas D., Lisker T., Olczak C., Spurzem R., Kotulla R., 2015, A&A, 576, A103
Bolton A. S., Burles S., Koopmans L. V. E., Treu T., Moustakas L. A., 2006, ApJ, 638, 703
Bolton A. S. et al., 2012, ApJ, 757, 82
Boselli A., Fossati M., Sun M., 2022, A&AR, 30, 3
Brodie J. P. et al., 2014, ApJ, 796, 52
Bundy K. et al., 2015, ApJ, 798, 7
Calvi R., Poggianti B. M., Vulcani B., Fasano G., 2013, MNRAS, 432, 3141
Cappellari M., 2002, MNRAS, 333, 400
Cappellari M., 2008, MNRAS, 390, 71
Cappellari M., 2017, MNRAS, 466, 798
Cappellari M., Copin Y., 2003, MNRAS, 342, 345
Cappellari M., Emsellem E., 2004, PASP, 116, 138
Cappellari M. et al., 2007, MNRAS, 379, 418
Cappellari M. et al., 2011, MNRAS, 413, 813
Cappellari M. et al., 2013a, MNRAS, 432, 1709
Cappellari M. et al., 2013b, MNRAS, 432, 1862
Cappellari M. et al., 2015, ApJ, 804, L21
Cebrián M., Trujillo I., 2014, MNRAS, 444, 682
Chabrier G., 2003, PASP, 115, 763
Croom S. M. et al., 2012, MNRAS, 421, 872
Deeley S. et al., 2017, MNRAS, 467, 3934
Derkenne C., McDermid R. M., Poci A., Remus R.-S., Jørgensen I., Emsellem E., 2021, MNRAS, 506, 3691
de Ravel L. et al., 2011, preprint (arXiv:1104.5470)
Dolag K., 2015, IAU General Assembly, 29, 2250156
Driver S. P. et al., 2011, MNRAS, 413, 971
Dubois Y., Devriendt J., Slyz A., Teyssier R., 2012, MNRAS, 420, 2662
Dubois Y. et al., 2014, MNRAS, 444, 1453
Emsellem E., Monnet G., Bacon R., 1994, A&A, 285, 723
Emsellem E. et al., 2011, MNRAS, 414, 888
Fabjan D., Borgani S., Tornatore L., Saro A., Murante G., Dolag K., 2010, MNRAS, 401, 1670
Foreman-Mackey D., Hogg D. W., Lang D., Goodman J., 2013, PASP, 125, 306
Foster C. et al., 2021, PASA, 38, e031
Grillo C. et al., 2015, ApJ, 800, 38
Gruen D. et al., 2013, MNRAS, 432, 1455
Grützbauch R., Conselice C. J., Varela J., Bundy K., Cooper M. C., Skibba R., Willmer C. N. A., 2011, MNRAS, 411, 929
Gunn J. E., Gott J. R., III, 1972, ApJ, 176, 1
Hartke J., Kakkad D., Reyes C., Moya-Sierralta C., Reyes A., Kravtsov T., Kolb J., Selman F., 2020, in Schreiber L., Schmidt D., Vernet E., eds, Proc. SPIE Conf. Ser. Vol. 11448, Adaptive Optics Systems VII., SPIE, Vol. 11448, Bellingham, p. 114480V
Hilz M., Naab T., Ostriker J. P., 2013, MNRAS, 429, 2924
Hirschmann M., Dolag K., Saro A., Bachmann L., Borgani S., Burkert A., 2014, MNRAS, 442, 2304
Ho M., Ntampaka M., Rau M. M., Chen M., Lansberry A., Ruehle F., Trac H., 2022, Nat. Astron., 6, 936
Hogg D. W., Foreman-Mackey D., 2018, ApJS, 236, 11
Jauzac M. et al., 2016, MNRAS, 463, 3876
Jeans J. H., 1922, MNRAS, 82, 122
Jian H.-Y., Lin L., Chiueh T., 2012, ApJ, 754, 26
Jones C., Forman W., 1984, ApJ, 276, 38
Kimmig L. C., Remus R.-S., Dolag K., Biffi V., 2022, preprint (arXiv:2209.09916)
Lagattuta D. J. et al., 2022, MNRAS, 514, 497
Lagos C. d. P., Schaye J., Bahé Y., van de Sande J., Kay S. T., Barnes D., Davis T. A., Dalla Vecchia C., 2018, MNRAS, 476, 4327
Lauer T. R. et al., 1995, AJ, 110, 2622
Leitherer C. et al., 1999, ApJS, 123, 3
Li R., Shu Y., Wang J., 2018, MNRAS, 480, 431
Li R. et al., 2019, MNRAS, 490, 2124
Lilly S. J. et al., 2007, ApJS, 172, 70
Limousin M., Kneib J. P., Bardeau S., Natarajan P., Czoske O., Smail I., Ebeling H., Smith G. P., 2007, A&A, 461, 881
Limousin M., Sommer-Larsen J., Natarajan P., Milvang-Jensen B., 2009, ApJ, 696, 1771
López-Sanjuan C. et al., 2015, A&A, 576, A53
Lotz J. M., Jonsson P., Cox T. J., Croton D., Primack J. R., Somerville R. S., Stewart K., 2011, ApJ, 742, 103
Lotz J. M. et al., 2017, ApJ, 837, 97
Maltby D. T. et al., 2010, MNRAS, 402, 282
Mann A. W., Ebeling H., 2012, MNRAS, 420, 2120
Maulbetsch C., Avila-Reese V., Colín P., Gottlöber S., Khalatyan A., Steinmetz M., 2007, ApJ, 654, 53
Mentz J. J. et al., 2016, MNRAS, 463, 2819
Merten J. et al., 2011, MNRAS, 417, 333
Mihos C., 2003, preprint (arXiv:astro-ph/0305512)
Moore B., Katz N., Lake G., Dressler A., Oemler A., 1996, Nature, 379, 613
Naab T., Johansson P. H., Ostriker J. P., 2009, ApJ, 699, L178
Navarro J. F., Frenk C. S., White S. D. M., 1997, ApJ, 490, 493
Nedkova K. V. et al., 2021, MNRAS, 506, 928
Oldham L. J., Auger M. W., 2018, MNRAS, 476, 133
Owers M. S., Couch W. J., Nulsen P. E. J., Randall S. W., 2012, ApJ, 750, L23
Papovich C. et al., 2012, ApJ, 750, 93
Pillepich A. et al., 2018, MNRAS, 473, 4077
Poci A., Cappellari M., McDermid R. M., 2017, MNRAS, 467, 1397
Poggianti B. M. et al., 2017, ApJ, 844, 48
Reiprich T. H., Böhringer H., 2002, ApJ, 567, 716
Remus R.-S., Burkert A., Dolag K., Johansson P. H., Naab T., Oser L., Thomas J., 2013, ApJ, 766, 71
Remus R.-S., Dolag K., Naab T., Burkert A., Hirschmann M., Hoffmann T. L., Johansson P. H., 2017, MNRAS, 464, 3742
Richard J., Kneib J. P., Limousin M., Edge A., Jullo E., 2010, MNRAS, 402, L44

Downloaded from https://academic.oup.com/mnras/article/522/3/3602/7152361 by Universiteit Leiden - LUMC user on 21 February 2024

Robotham A. S. G., Davies L. J. M., Driver S. P., Koushan S., Taranu D. S., Casura S., Liske J., 2018, MNRAS, 476, 3137
Ruff A. J., Gavazzi R., Marshall P. J., Treu T., Auger M. W., Brault F., 2011, ApJ, 727, 96
Salpeter E. E., 1955, ApJ, 121, 161
Schwarzschild M., 1979, ApJ, 232, 236
Schwinn J., Jauzac M., Baugh C. M., Bartelmann M., Eckert D., Harvey D., Natarajan P., Massey R., 2017, MNRAS, 467, 2913
Scott N. et al., 2013, MNRAS, 432, 1894
Scott T. C., Brinks E., Cortese L., Boselli A., Bravo-Alfaro H., 2018, MNRAS, 475, 4648
Serra P., Oosterloo T., Cappellari M., den Heijer M., Józsa G. I. G., 2016, MNRAS, 460, 1382
Shankar F., Marulli F., Bernardi M., Mei S., Meert A., Vikram V., 2013, MNRAS, 428, 109
Sharma G., Salucci P., van de Ven G., 2022, A&A, 659, A40
Simionescu A., Werner N., Mantz A., Allen S. W., Urban O., 2017, MNRAS, 469, 1476
Smith R., Choi H., Lee J., Rhee J., Sanchez-Janssen R., Yi S. K., 2016, ApJ, 833, 109
Sonnenfeld A., Treu T., Gavazzi R., Suyu S. H., Marshall P. J., Auger M. W., Nipoti C., 2013, ApJ, 777, 98
Soto K. T., Lilly S. J., Bacon R., Richard J., Conseil S., 2016, MNRAS, 458, 3210
Springel V., 2010, MNRAS, 401, 791
Springel V., Hernquist L., 2003, MNRAS, 339, 289
Springel V., Di Matteo T., Hernquist L., 2005a, MNRAS, 361, 776
Springel V. et al., 2005b, Nature, 435, 629
Stone R. P. S., 1996, ApJS, 107, 423
Teyssier R., 2002, A&A, 385, 337
Thomas J. et al., 2011, MNRAS, 415, 545
Valdes F., Gupta R., Rose J. A., Singh H. P., Bell D. J., 2004, ApJS, 152, 251
Vazdekis A., Sánchez-Blázquez P., Falcón-Barroso J., Cenarro A. J., Beasley M. A., Cardiel N., Gorgas J., Peletier R. F., 2010, MNRAS, 404, 1639
Wang Y. et al., 2019, MNRAS, 490, 5722
Wang Y. et al., 2020, MNRAS, 491, 5188
Watson C. et al., 2019, ApJ, 874, 63
Weilbacher P. M. et al., 2020, A&A, 641, A28
Weinberger R. et al., 2018, MNRAS, 479, 4056
Williamson R. et al., 2011, ApJ, 738, 139
Zheng W. et al., 2012, Nature, 489, 406
Zitrin A., Broadhurst T., 2009, ApJ, 703, L132

APPENDIX A: VALIDATION OF MUSE-BASED MGES

The JAM method has previously assumed the availability of high-resolution photometric data from which stellar MGEs are obtained. The MAGPI survey currently has no space-based imaging for its targets (aside from the two archival Frontier Fields clusters), and so the highest resolution imaging available is actually synthetic images constructed from the IFU data themselves. Even with GLAO, the PSF FWHM of the MAGPI fields is around 10 times larger than that of, e.g. *HST* data. The pixel scale is also around seven times larger for MUSE data than *HST*, comparing the 0.2 arcsec per pixel size of MUSE for the MAGPI fields to the 0.03 arcsec per pixel size of the *HST* data of the supplementary MAGPI fields, Abell 2744 and Abell 370. In this section, we investigate how this difference in resolution and pixel scale affects the resulting MGEs and derived inner density slopes.

To explore this issue, we completed end-to-end simulations of the JAM modelling process with mock galaxies 'observed' with a MUSE pixel scale, MAGPI-like noise for the photometry and kinematics, and a PSF FWHM of 0.6 arcsec. A MGE measured from a galaxy in Abell 2744 from the Frontier Fields sample with *HST* photometry

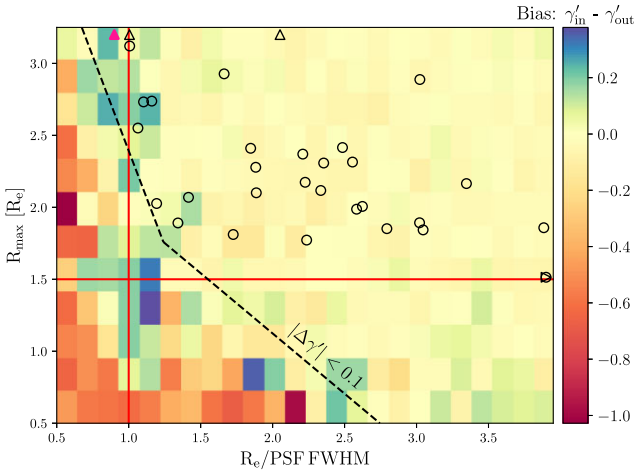

Figure A1. The results of the end-to-end simulations for the parameter γ', the inner density slope of the total potential. The *y*-axis shows the extent of the kinematic coverage expressed as a fraction of the effective radii. The *x*-axis shows the effective radius as a fraction of the PSF FWHM of the data used to measure the MGEs. The yellow region is where the input inner density slope is well recovered. The red lines indicate the cuts used to define the sample in this work (upper right quadrant, with a median shift of 1 per cent towards shallower slopes). The black dashed line shows where the absolute bias is less than 0.1. The sample of 30 MAGPI galaxies are shown as black circles, with arrow markers indicating points off the plot region (3 objects). The pink triangle shows the test data case, object 4423 from Abell 2744.

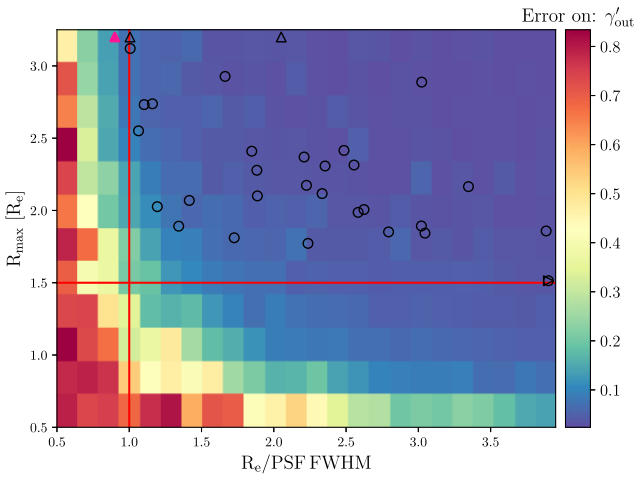

Figure A2. The same as Fig. A1, however instead showing the standard deviation of the EMCEE posterior distribution for the inner density slope. The blue region indicates the parameter space for which the inner density slope is well constrained. The upper right quadrant as defined by the red lines has a median uncertainty of ± 0.03 on γ'. The sample of 30 MAGPI galaxies are shown as black circles, with arrow markers indicating points off the plot region (3 objects). The pink triangle shows the test data case, object 4423 from Abell 2744.

was used as the underlying MGE from which all others were created. The suite of mock galaxies were made by scaling the Gaussian sigmas to change the effective radius, and scaling the Gaussian heights to change the surface density. The MGEs were scaled so that all mock galaxies fall on the *HST*-CANDELS mass–size relation for redshifts $z = 0.2-(-0.5)$ (Nedkova et al. 2021).

Two parameters were used to investigate whether a MUSE-based MGE could recover the inner density slope (γ') without bias. We

Downloaded from https://academic.oup.com/mnras/article/522/3/3602/7152361 by Universiteit Leiden - LUMC user on 21 February 2024

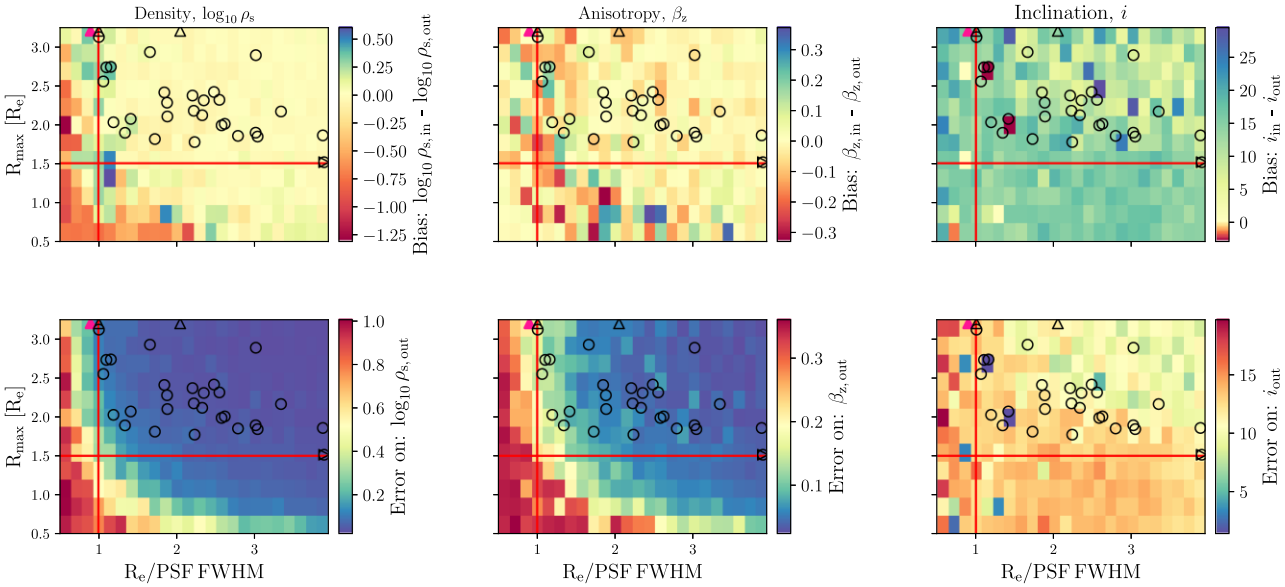

Figure A3. Same as Figs A1 and A2, however for the other three parameters used when constructing dynamical models in this work. The density at the break radius, $\log_{10}\rho_s$, orbital anisotropy, β_z, and inclination, i. The red lines indicate the parameter cuts used to select the final MAGPI sample. The top row shows the bias estimated when recovering each parameter, and the bottom row shows the standard deviation of the EMCEE posterior distribution. The pink triangle shows the test data case, object 4423 from Abell 2744.

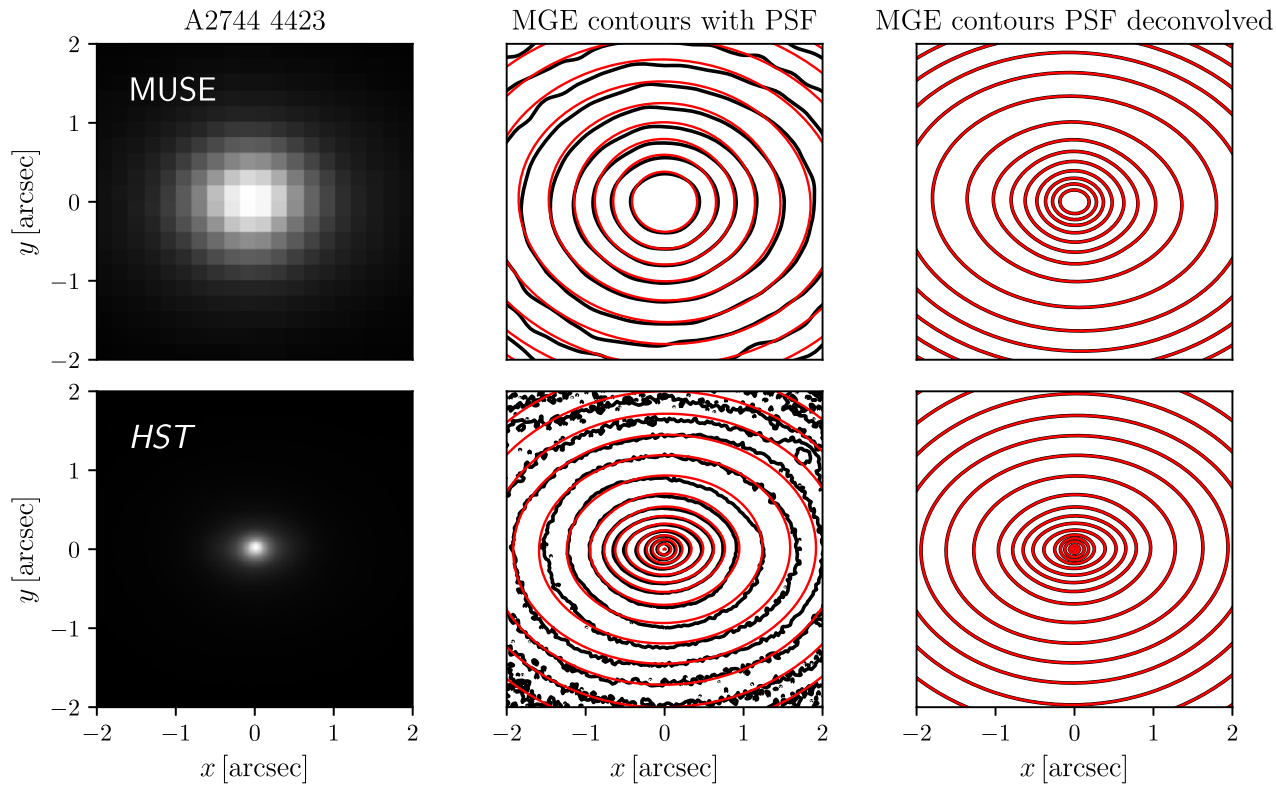

Figure A4. Top row: The SDSS *r*-band 'image' made from the MUSE data cube for galaxy A2744 4423, and the associated MGE fit contours (red) overlaid on the galaxy isophotes (black). The third column shows the MUSE PSF deconvolved galaxy surface brightness model. Bottom row: The *F814W* filter *HST* thumbnail of A2744 4423, and associated MGE fit (red) overlaid on the galaxy isophotes (black), in steps of 0.5 mag per square arcsecond. The third column shows the *HST* PSF deconvolved galaxy surface brightness model.

choose to focus on the recovery of the inner density slope as it closely correlates to the total density slope, aside from the radial bounds used as described in Section 3.4. The parameters we investigated are (1) The effective radius as a fraction of the PSF FWHM and (2) the radial extent of the kinematic data R_{max}, expressed as a fraction of the effective radius. A suite of 288 mock galaxies were created,

Downloaded from https://academic.oup.com/mnras/article/522/3/3602/7152361 by Universiteit Leiden - LUMC user on 21 February 2024

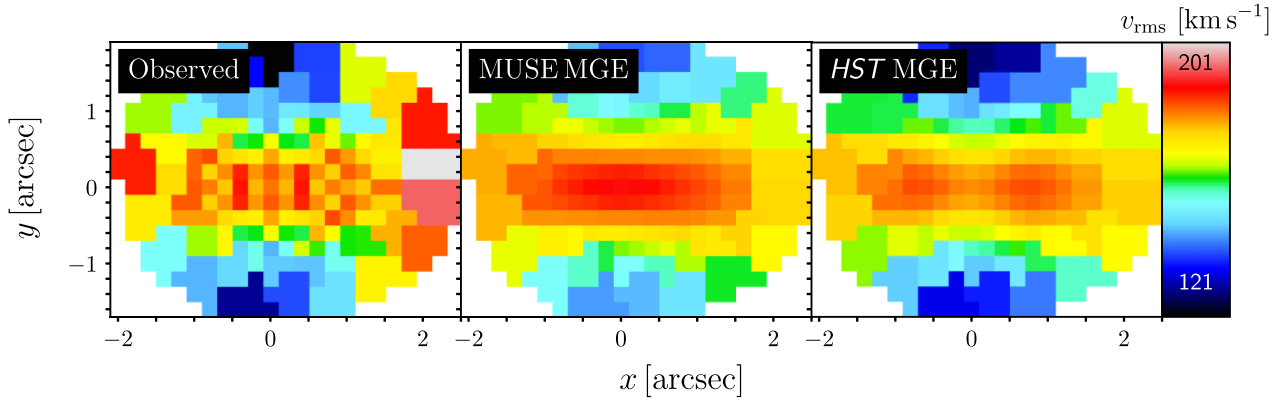

Figure A5. The left-hand panel shows the observed $v_{\rm rms}$ field for galaxy Abell 2744 4423. The middle panel shows the $v_{\rm rms}$ field generated from the median of the posterior distribution using JAM and a MUSE-based MGE. The right-hand panel shows the same, but for a modelled $v_{\rm rms}$ field using JAM and a *HST*-based MGE. The *HST*-based model recovered $\gamma' = -2.087 \pm 0.02$ and the MUSE-based model recovered $\gamma' = -2.089 \pm 0.04$.

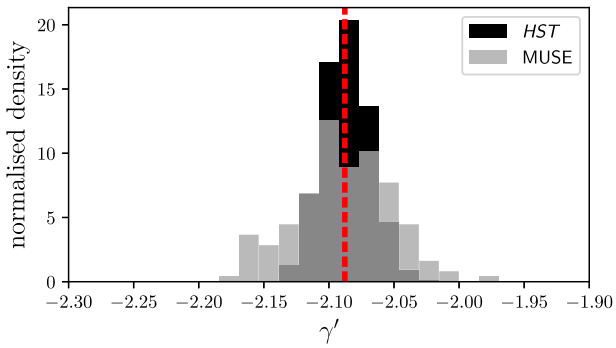

Figure A6. The normalized posterior distribution from EMCEE for the inner density slope using MUSE and *HST*-based MGEs. A red dashed line indicates the median of each distribution, but overlaps as the recovered inner density slopes are near identical.

spanning 0.5–3.95 in $R_{\rm e}$/PSF FWHM and 0.5–3.25 in $R_{\rm max}/R_{\rm e}$. Each of the 288 mock galaxies is an independent 'observation' due to the random noise added to both the photometry before the MGEs were measured and the $v_{\rm rms}$ fields before JAM modelling.

Each mock galaxy image was convolved with the adopted PSF, as if it were observed. Adding noise to the photometry and kinematics was informed by MAGPI data, ensuring a realistic treatment. A relationship between noise (from the MAGPI data) and surface brightness (from MAGPI galaxies) was created. The value of noise at each surface brightness was treated as the sigma of a Gaussian distribution, so that MAGPI-like noise could be randomly drawn from that Gaussian distribution and added on to the model galaxies before MGEs were measured.

For the $v_{\rm rms}$ fields a similar process was used. The underlying scaled MGE (without noise or PSF convolution) was used to create a $v_{\rm rms}$ field, which was then convolved with the adopted PSF. Measured uncertainties in velocity and velocity dispersion, as described in Section 3.2, were used to create a relationship between surface brightness of MAGPI galaxies and $v_{\rm rms}$ noise in km s^{-1}. This relationship was used to again add noise to the model input $v_{\rm rms}$ fields based on the surface brightness of the modelled galaxy.

Models of the second velocity moments were then constructed using these mock luminous MGEs and mock $v_{\rm rms}$ fields as if they were observed data, following exactly the method outlined in Section 3.3. As with actual MAGPI data, the constrained parameters are from PSF-deconvolved models. These simulations show in what circumstances the PSF-deconvolved MGE surface brightness model is not an accurate description of the underlying galaxy, and therefore constrains a biased total density profile.

The difference between the known, input inner density slopes and the recovered inner density slopes is shown in Fig. A1. The results of the simulation show that there is a compromise between having kinematic data across a large radial extent and having a well-resolved effective radius compared to the PSF FWHM of observation. Poorly resolved galaxies with $1R_{\rm e}$ comparable to the PSF FWHM, but with multiple effective radii of kinematic coverage, return the inner density slope with little bias (upper left regions in yellow of Fig. A1). However, the opposite is also apparent; galaxies that are *well* resolved but with small radial coverage for the kinematics do not recover the input inner density slope well (e.g. bottom row of Fig. A1). The errors expressed as a standard deviation of the EMCEE posterior distribution are shown in Fig. A2.

Based on the results of these end-to-end simulations, we make simple cuts in the parameter space as a data-quality requisite for MAGPI galaxies included in the final sample. These cuts are shown as red lines in both Figs A1 and A2. On Fig. A1, we also show a dashed line to indicate where the input and recovered inner density slope have an absolute difference of less than 0.1, after smoothing. To make the final sample, a MAGPI object must have $R_{\rm e}$/PSF FWHM > 1 and $R_{\rm max}/R_{\rm e} > 1.5$. Although a curve or some other more complex function encapsulates the unbiased and well-constrained region of the simulations more accurately, it is not necessary given the distribution of MAGPI objects in this parameter space. The chosen cuts result in a median difference between $\gamma'_{\rm in}$ and $\gamma'_{\rm out}$ of 1 per cent towards shallower (less negative) slopes, and a median uncertainty of ± 0.03 on $\gamma'_{\rm out}$. Here, we show only the results for γ'; however, for the chosen cuts the other parameters used in the JAM models (ρ, β_z, and i) are also recovered with comparable accuracy. Making a more stringent data cut of $R_{\rm e}$/PSF FWHM > 1.5 does not change the results claimed in this work, resulting in a sample of 21 galaxies and median $\gamma = -2.22 \pm 0.05$, or 14 galaxies when also excluding spiral galaxies with median $\gamma = -2.22 \pm 0.04$.

The cuts imply a certain level of bias in the sample selection of MAGPI objects used in this work. Well-resolved objects with kinematic data that extends less than $1.5R_{\rm e}$ imply low-mass, faint galaxies are excluded from the sample. This is not an issue when comparing the MAGPI and Frontier Fields samples, as we only compare against Frontier Fields objects with the same radial coverage

Downloaded from https://academic.oup.com/mnras/article/522/3/3602/7152361 by Universiteit Leiden - LUMC user on 21 February 2024

of kinematic data, as described in Section 3.4. For the other extreme, compact objects that are poorly resolved are also preferentially removed from the selected sample based on the cuts made here. As compact objects tend to have steeper (more negative) total density slopes, we do not expect this cut to influence our conclusion of an observed difference in the distributions of total density slopes between the MAGPI and Frontier Fields galaxies.

The entire modelling process was repeated with a different underlying MGE (with a more elliptical morphology) and with different input parameters (e.g. a different input galaxy inclination, inner density slope, density at the break radius, and anisotropy). The simulation results shown in Figs A1 and A2 are indicative of those for these different underlying MGEs and parameter sets. In Fig. A3, we show the simulation results for the remaining parameters. Inclination is recovered the worst, although this parameter is not used for the density slope calculation.

Given some of the Frontier Fields already have existing *HST* and MUSE data, and an effective radius that approximates the MUSE PSF size, it is possible to test the accuracy of this simulation process. We show a comparison between the inner regions of a MUSE-based and *HST*-based MGE for the Abell 2744 galaxy used to create all the mock galaxies in Fig. A4, which was modelled in Derkenne et al. (2021). The *HST*-based MGE model clearly has more structure visible than the MUSE-based MGE model, the inner regions of which are noticeably blurred by the PSF compared to the *HST* model on the same scale. Although the PSF deconvolved models using *HST* and MUSE data are similar they are not identical, which is what motivated the end-to-end simulation process using mock galaxies. The observed and modelled $v_{\rm rms}$ fields using the MUSE-based and *HST*-based MGEs are shown in Fig. A5.

As with the MGEs, the JAM model using the *HST* stellar MGE and MUSE kinematics exhibits more structure than the MUSE-based model. However, the MUSE-based model of this galaxy is able to return an almost identical parameter set to the *HST*-based model. The recovered inner density slope from both models are shown in Fig. A6, with a median of $\gamma' = -2.087 \pm 0.02$ using *HST* data and $\gamma' = -2.089 \pm 0.04$ using MUSE data. The other three parameters were recovered for MUSE (*HST*) data as $\log \rho_{\rm s} = -2.76 \pm 0.03$ (-2.80 ± 0.02), $\beta_z == -0.47 \pm 0.04$ (-0.45 ± 0.04), and $i = 71 \pm 9$ (79 ± 9) degrees. The galaxy A2744 4423 has $R_{\rm e}$ as a fraction of the MUSE PSF FWHM of ~0.9 and $R_{\rm max}/R_{\rm e}$ of ~3.7, which demonstrates well the compromise between resolution and kinematic coverage on recovering the inner density slope (and the other parameters used to create the JAM models) discussed above.

APPENDIX B: IMPACT OF RADIAL BOUNDS AND BREAK RADIUS ON THE TOTAL SLOPE

To construct the dynamical models in this work, we have assumed a break radius (the radius at which the total density profile transitions from a free inner slope to a fixed outer slope of −3) is 20 kpc. This choice was motivated to be consistent with other dynamical modelling works (Cappellari et al. 2015; Poci et al. 2017; Bellstedt et al. 2018; Derkenne et al. 2021), as it is expected the derived total slope will vary systematically with the break radius.

We re-ran the MAGPI JAM models using two other choices of break radius to explore the impact of this parameter on the derived total density slopes; 10 and 30 kpc. The results of this test are shown in Fig. B1.

The total density slopes derived when using a break radius of 20 kpc or 30 kpc are generally consistent within errors, with median derived total density slope $\gamma = -2.22 \pm 0.05$ and $\gamma = -2.22 \pm 0.04$,

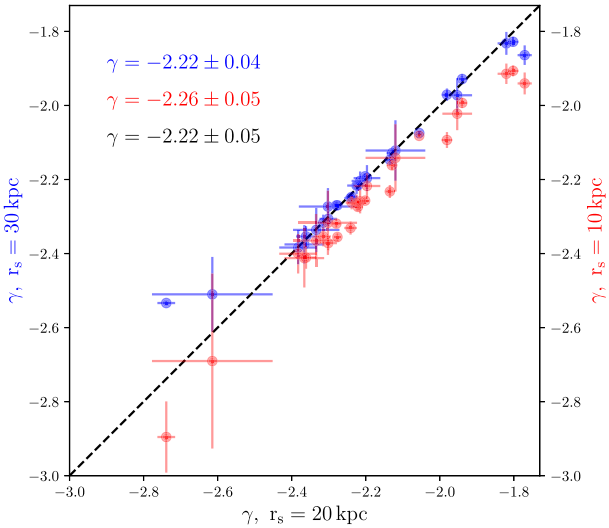

Figure B1. The total density slope, γ, derived with different choices of break radius, $r_{\rm s}$: 10, 20, and 30 kpc. The median gamma values with standard error on the median are inset. There is no difference in the derived median density slope for break radii values of 20 and 30 kpc; however, the derived density slopes for a break radius of 10 kpc are on average steeper than those derived with a break radius of 20 kpc.

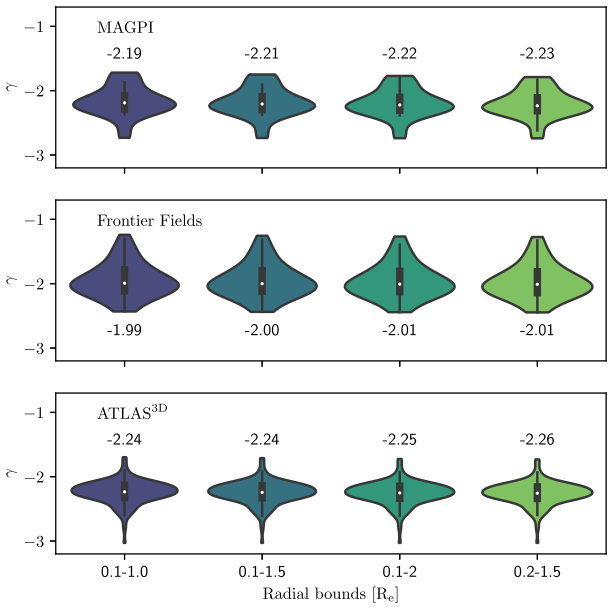

Figure B2. A 'violin' plot showing the slope distributions of the MAGPI, Frontier Fields, and ATLAS$^{\rm 3D}$ samples, for four different choices of radial bounds: $r = [R_{\rm e}/10, 1\,R_{\rm e}]$, $r = [R_{\rm e}/10, 1.5\,R_{\rm e}]$, $r = [R_{\rm e}/5, 1.5\,R_{\rm e}]$, and $r = [R_{\rm e}/10, 2\,R_{\rm e}]$. The choice of radial bounds $r = [R_{\rm e}/10, 2\,R_{\rm e}]$ is the one on which we base our conclusions in the main text. The violin plots shows a kernel density estimate of the underlying points. A box plot is inset with whiskers set to 1.5 the interquartile range. The median total density slope is shown as a white dot, and is also annotated above each data set.

respectively. A break radius of 10 kpc results in steeper slopes on average, as the transition between a free slope and a fixed outer slope of −3 physically occurs at smaller radii for each galaxy. The median with the break radius set as 10 kpc is $\gamma = -2.26 \pm 0.05$. We conclude that setting the break radius to smaller than 20 kpc systematically

Downloaded from https://academic.oup.com/mnras/article/522/3/3602/7152361 by Universiteit Leiden - LUMC user on 21 February 2024

drives the slopes to steeper values, and setting the break radius to values larger than 20 kpc has no significant effect.

Another potential source of systematic bias in this work is the choice of radial bounds when computing the total density slope. We have computed all MAGPI, Frontier Fields and ATLAS^{3D} slopes on the radial range of $r = [R_e/10, 2\,R_e]$. As a double power law is used to describe the total density profile, the exact choice of radial bounds will necessarily have an effect on the derived median slope.

To test the impact of the radial bounds when computing total density slopes we re-calculated all the slopes for the MAGPI, Frontier Fields, and ATLAS^{3D} samples on three other radial ranges in addition to the ones reported in the main text. In total, the four radial ranges tested are $r = [R_e/10, 1\,R_e]$, $r = [R_e/10, 1.5\,R_e]$, $r = [R_e/5, 1.5\,R_e]$, and $r = [R_e/10, 2\,R_e]$.

We show the results of this test as a 'violin' plot in Fig. B2. As the outer radial bound gets larger the derived median density slope becomes marginally steeper. As discussed above, this is because the outer fixed slope of -3 influences the total derived slope at physical radii around 20 kpc. However, the difference between the derived median density slopes for these choices of radial bounds are minimal, and the relative trends between them are maintained. That is, the Frontier Fields slopes remain significantly more shallow than either the MAGPI or ATLAS^{3D} samples for all choices of radial bounds. The shape of the distribution for different radial bounds is also constant. Finally, the change in the median slope for these different bound is consistent with the quoted uncertainty on the total density slope (± 0.05 for MAGPI).

We note that the radial range of $r = [R_e/10, 1\,R_e]$ (first column on Fig. B2) is most similar to the radial ranges used in the majority of gravitational lensing works (see Table C2 in Appendix C for a summary), as the Einstein radius generally approximates an effective radius.

APPENDIX C: TABULATED TOTAL SLOPES

We present the tabulated results for the MAGPI sample in Table C1, including their IDs, coordinates, redshift, central velocity dispersion, total mass (defined as twice the mass integrated within a sphere of $1R_e$), the circularized effective radius, total density slope, and associated uncertainties.

Table C2 summaries the median total density slopes are measured by various works, and includes all studies as shown on Fig. 8. In particular, we give the redshift, sample size, total density slope, and radial range across which the slope was measured or constrained.

Table C1. Columns 1–4: The MAGPI ID, right ascension and declination, and redshift of each object used in this work. The Field of each object corresponds to the first 4 numbers of the MAGPI ID. Column 5: The measured $1R_e$ aperture velocity dispersion from the kinematics. Column 6: Twice the mass integrated within a sphere of $1R_e$ using the median total potential parametrization from the EMCEE posterior distribution, as described in Section 3.4. Column 7: The circularized effective radius containing half the galaxy light. Column 8: The average density slope measured between $0.1R_e$ and $2R_e$ for each galaxy. Columns 9 and 10: The 16th and 84th percentiles offset from the 50th percentile of the EMCEE posterior distribution. These are Monte Carlo errors as described in Section 3.4. No uncertainties are given for the central dispersion or effective radius as these measurements are dominated by systematic effects.

MAGPI ID (1)	RA (J2000) (2)	Decl. (J2000) (3)	z (4)	σ_e (km s^{-1}) (5)	$\log_{10}(M/M_\odot)$ (6)	R_e (kpc) (7)	γ (8)	+err (9)	−err (10)
1202197197	175.3388	−1.5825	0.2920	148	11.4 ± 0.01	7.68	−1.82	0.02	0.03
1203040085	175.3562	0.6272	0.3132	271	11.4 ± 0.04	3.34	−2.33	0.06	0.06
1203060081	175.3549	0.6268	0.2799	203	11.0 ± 0.01	2.49	−2.12	0.08	0.09
1203070184	175.3549	0.6323	0.3089	223	11.5 ± 0.02	6.02	−2.22	0.02	0.02
1203087201	175.3535	0.6335	0.3094	108	10.6 ± 0.03	3.16	−2.30	0.08	0.08
1203196196	175.3474	0.6333	0.3103	299	12.0 ± 0.01	9.23	−1.94	0.01	0.01
1203230310	175.3456	0.6396	0.3120	162	10.9 ± 0.01	2.99	−2.20	0.04	0.03
1203305151	175.3413	0.6308	0.3152	241	11.2 ± 0.01	2.61	−2.38	0.05	0.05
1204141177	175.6646	−0.7958	0.1070	177	10.9 ± 0.00	2.22	−2.06	0.00	0.01
1204198199	175.6615	−0.7946	0.3164	163	11.4 ± 0.00	7.94	−1.80	0.01	0.02
1205093221	178.0856	−0.8259	0.2918	189	11.2 ± 0.01	5.01	−2.30	0.02	0.03
1205196165	178.0798	−0.8290	0.2925	81	10.4 ± 0.03	3.28	−2.17	0.14	0.17
1205197197	178.0798	−0.8272	0.2919	97	10.9 ± 0.02	7.43	−2.28	0.02	0.03
1206110186	180.1670	−1.4530	0.2677	264	11.7 ± 0.00	6.73	−2.20	0.01	0.01
1206196198	180.1622	−1.4524	0.3271	255	11.7 ± 0.00	8.81	−2.28	0.01	0.01
1206276211	180.1578	−1.4516	0.2689	206	11.3 ± 0.01	5.10	−2.22	0.03	0.03
1207128248	182.0037	−2.4805	0.3215	170	11.2 ± 0.01	4.91	−2.37	0.05	0.06
1207197197	181.9999	−2.4834	0.3212	103	10.8 ± 0.01	6.63	−2.36	0.03	0.05
1208197197	184.9718	−2.4811	0.3008	208	11.4 ± 0.01	5.03	−2.13	0.01	0.01
1209131247	185.6022	−1.3774	0.2960	155	11.0 ± 0.01	3.50	−1.95	0.04	0.05
1209197197	185.5985	−1.3801	0.2960	159	11.2 ± 0.09	5.86	−2.13	0.01	0.01
1209206324	185.5981	−1.3731	0.5710	177	11.0 ± 0.04	4.58	−2.61	0.16	0.19
1501196198	212.3056	1.7839	0.3100	242	11.9 ± 0.03	10.54	−1.98	0.01	0.02
1501224275	212.3040	1.7882	0.3118	158	10.7 ± 0.01	2.91	−2.74	0.02	0.04
1507196198	215.6209	0.4080	0.3152	213	11.2 ± 0.00	4.16	−2.31	0.02	0.02
1508197198	215.8838	2.7133	0.3164	177	11.2 ± 0.01	5.31	−1.77	0.02	0.02
1523197197	219.5414	−1.0993	0.2813	184	11.3 ± 0.01	5.75	−2.28	0.01	0.01
1525170222	219.6684	0.3349	0.3210	327	11.7 ± 0.04	5.52	−2.24	0.02	0.01
1525196197	219.6669	0.3335	0.3187	228	11.5 ± 0.01	6.15	−2.22	0.01	0.01
1530197196	222.1438	2.9410	0.3108	288	11.3 ± 0.04	2.49	−2.24	0.02	0.01

Downloaded from https://academic.oup.com/mnras/article/522/3/3602/7152361 by Universiteit Leiden - LUMC user on 21 February 2024

Table C2. A summary of the literature total density slopes values shown in Fig. 8. All values are calculated as a median unless except for Bolton et al. (2012) where the fitted relation is given, and Li et al. (2018) where the mean is given. Column 1 gives the sample and study from which the slopes are drawn. Note that slopes from Derkenne et al. (2021), Poci et al. (2017), Bellstedt et al. (2018), and Thomas et al. (2011) were all re-analysed to be on the same radial range as MAGPI total density slopes. Column 2: The redshift range or value. Column 3: The sample size of galaxies. Column 4: The radial range across which the total density slope was measured. Column 5: The median total density slope with the standard error on the median. Column 6: The standard deviation of the sample total density slopes.

Sample (1)	z (2)	N (3)	Radial range (4)	Median γ (5)	σ_γ (6)
Dynamics					
MAGPI (this work)	0.31	28	$0.1\,R_e$–$2\,R_e$	-2.22 ± 0.05	0.22
Frontier Fields (Derkenne et al. 2021)	$0.29 < z < 0.55$	64	$0.1\,R_e$–$2\,R_e$	-2.01 ± 0.04	0.26
ATLAS^{3D} (Poci et al. 2017)	~0	150	$0.1\,R_e$–$2\,R_e$	-2.25 ± 0.02	0.17
Coma (Thomas et al. 2011)	0.0231	17	$0.1\,R_e$–$2\,R_e$	-2.00 ± 0.06	0.20
SLUGGS (Bellstedt et al. 2018)	~0	22	$0.1\,R_e$–$2\,R_e$	-2.06 ± 0.04	0.13
MaNGA (Li et al. 2019)	~0	2110	$<R_e$	-2.22 ± 0.006	0.22
Simulations					
Magneticum (Remus et al. 2017)	0.34	93	$0.4\,R^{3D}_{1/2}$–$4\,R^{3D}_{1/2}$	-2.11 ± 0.02	0.16
Magneticum (Remus et al. 2017)	0.066	96	$0.4\,R^{3D}_{1/2}$–$4\,R^{3D}_{1/2}$	-2.05 ± 0.016	0.13
IllustrisTNG (Wang et al. 2019)	~0	559	$0.4\,R^{3D}_{1/2}$–$4\,R^{3D}_{1/2}$	-2.00 ± 0.0004	0.17
IllustrisTNG (Wang et al. 2019)	0.3	731	$0.4\,R^{3D}_{1/2}$–$4\,R^{3D}_{1/2}$	-1.98 ± 0.0086	0.19
Horizon-AGN	0.018	2659	$0.1\,R_e$–$2\,R_e$	-1.99 ± 0.004	0.17
Horizon-AGN	0.305	2170	$0.1\,R_e$–$2\,R_e$	-1.93 ± 0.004	0.15
Lensing					
SLACS (Auger et al. 2010)	$0.063 < z < 0.358$	58	$<R_{\rm Einstein}$	-2.09 ± 0.04	0.22
SLACS (Barnabè et al. 2011)	$0.0808 < z < 0.3475$	16	$<R_e$	-2.079 ± 0.05	0.16
SL2S (Ruff et al. 2011)	$0.238 < z < 0.65$	11	$<R_{\rm Einstein}$	-2.09 ± 0.11	0.29
SLACS and BELLS (Bolton et al. 2012)	$0.1 < z < 0.6$	85	$<R_{\rm Einstein}$	$\gamma(z) = (-2.11 \pm 0.02) + z(0.6 \pm 0.15)$	–
SL2S (Sonnenfeld et al. 2013)	$0.238 < z < 0.78$	25	$<R_{\rm Einstein}$	-2.01 ± 0.05	0.21
BELLS, BELLS GALLERY, and SL2S (Li et al. 2018)	~0.5	63	$< 3\,R_e$	$\langle\gamma\rangle = -2.00 \pm 0.03$	0.18

[1]*Research Centre for Astronomy, Astrophysics, and Astrophotonics, School of Mathematical and Physical Sciences, Macquarie University, NSW 2109, Australia*
[2]*ARC Centre of Excellence for All Sky Astrophysics in 3 Dimensions (ASTRO 3D), Australia*
[3]*Centre for Extragalactic Astronomy, University of Durham, Stockton Road, Durham DH1 3LE, UK*
[4]*Research School of Astronomy and Astrophysics, Australian National University, Canberra, ACT 2611, Australia*
[5]*Kavli Institute for Cosmology, University of Cambridge, Madingley Road, Cambridge CB3 0HA, UK*
[6]*Cavendish Laboratory – Astrophysics Group, University of Cambridge, 19 JJ Thompson Avenue, Cambridge CB3 0HE, UK*
[7]*Department of Astronomy and Yonsei University Observatory, Yonsei University, Seoul 03722, Republic of Korea*
[8]*Universiäts-Sternwarte, Fakulät für Physik, Ludwig-Maximilians-Universität München, Scheinerstr. 1, D-81679 München, Germany*
[9]*International Centre for Radio Astronomy Research, The University of Western Australia, 35 Stirling Highway, Crawley, WA 6009, Australia*
[10]*Sydney Institute for Astronomy, School of Physics, Building A28, The University of Sydney, NSW 2006, Australia*
[11]*Instituto de Astrofísica de Canarias, IAC, Vía Láctea s/n, E-38205 La Laguna (S.C. Tenerife), Spain*
[12]*Departamento de Astrofísica, Universidad de La Laguna, E-38206 La Laguna (S.C. Tenerife), Spain*
[13]*School of Physics, University of New South Wales, Sydney, NSW 2052, Australia*
[14]*Cosmic Dawn Center (DAWN)*
[15]*Department of Astronomy, School of Physics, Peking University, 5 Yiheyuan Road, Beijing 100871, People's Republic of China*
[16]*Kavli Institute for Astronomy and Astrophysics, Peking University, 5 Yiheyuan Road, Beijing 100871, People's Republic of China*
[17]*Leiden Observatory Leiden University, PO Box 9513, NL-2300 RA Leiden, the Netherlands*
[18]*GSKY, INFN-Sezione di Trieste, via Valerio 2, I-34127 Trieste, Italy*
[19]*SISSA International School for Advanced Studies, via Bonomea 265, I-34136 Trieste, Italy*
[20]*Department of Physics and Astronomy, University of the Western Cape, Cape Town 7535, South Africa*
[21]*School of Mathematics and Physics, University of Queensland, Brisbane, QLD 4072, Australia*
[22]*Centre for Astrophysics and Supercomputing, School of Science, Swinburne University of Technology, Hawthorn, VIC 3122, Australia*

This paper has been typeset from a TEX/LATEX file prepared by the author.

© 2023 The Author(s)
Published by Oxford University Press on behalf of Royal Astronomical Society

Downloaded from https://academic.oup.com/mnras/article/522/3/3602/7152361 by Universiteit Leiden - LUMC user on 21 February 2024